2011

Preparation of Thermoelectric Nanocrystals for Energy Applications

Weijie Yu
Iowa State University

Preparation of thermoelectric nanocrystals for energy applications

by

Weijie Yu

A thesis submitted to the graduate faculty
in partial fulfillment of the requirements for the degree of

MASTER OF SCIENCE

Major: Materials Science and Engineering

Program of Study Committee:

Zhiqun Lin, Major Professor

Kaitlin Bratlie

Xinwei Wang

Daniel Attinger

Iowa State University

Ames, Iowa

2011

Table of Contents

Acknowledgements

I would like to thank my Major Professor, Dr. Zhiqun Lin, for the time and guidance he provided to me throughout my thesis work. Thanks to my committee member, Dr. Xinwei Wang, for his help on thermal conductivity test of my samples. Thanks to Dr. Kaitlin Bratlie and Dr. Daniel Attinger for being my committee members and promote my thesis. Special thanks to Dr. Scott Beckman for helping me with the theory of thermoelectric. Also thanks to my group members who helped me in this research. Former group members, Dr. Jun Wang and Dr. Ming He, gave me many constructive suggestions. And thanks to my current group member, Dr. Xinchang Pang, for teaching me the synthesis method for nanoparticles, and Xukai Xin and Jeahan Jung, for conducting TEM imaging. Additionally, I thank to other group members: Lei Zhao, Wei Han, Katie Schlichting, Bo Li, Hsiang-Yu Liu, Chaowei Feng for the support they gave me.

Importantly, I want to thank my family and friends. For my parents, who supported my life in Ames and always listened to and guided me wherever I was, I am really grateful forever. For my friends, Shuguo Xu and Hongchao Wu, who helped me a lot with the life in Ames, I am deeply appreciated.

Abstract

Thermoelectric materials, in which a temperature difference creates an electric potential or an electric potential creates a temperature difference, are probably a key to solving global warming and energy shortage problems. There are three thermoelectric effects: the Seebeck effect (temperature to current), Peltier effect (current to temperature), and Thomson effect (conductor heating/cooling). However the efficiency of thermoelectric materials has been rather low for practical applications, including power generation and refrigeration as it requires an optimization of the combination of conflicting material characteristics (i.e., thermal conductivity and electrical conductivity). To date, efforts have been made to capitalize on nanotechnology to create novel semiconducting materials that could finally make thermoelectricity a widely used technology. In my research, I systematically synthesized bismuth (Bi) nanocrystals as one of very important thermoelectric materials by hydrothermal and star-like amphiphilic block copolymer nanoreactor approaches. The size of Bi nanoparticles prepared by employing star-like amphiphilic block copolymer templates was better controlled. The thermoelectric properties of Bi nanocrystals were improved when their crystalline sizes are smaller than 10nm.

Chapter 1. Introduction

1.1. World Energy Problem & history of thermoelectric

Since last century, the technology explosion brings human a lot of convenience, like electrical appliances, vehicles, aircrafts as well as increasing energy consumption. Currently oil and coal are still the most important energy in the world, which will be depleted in a few decades. On the other hand, the environmental pollution caused by burning fossil fuel is becoming more and more critical. Developing thermoelectric power generation devices is a promising way to solve this energy and pollution problems. Most machines and electrical appliances generate a great amount waste heat when they are working, while thermoelectric devices can gathering the waste heat and convert it into electricity.

1.2. Seebeck Effect

Thermoelectric effect includes Seebeck Effect, Peltier Effect and Thomson Effect[1]. It is defined as the direct conversion between heat energy and electric energy. A temperature difference applied on the two side of a thermoelectric device can generate a voltage difference, vice versa. Due to these attractive features, thermoelectric materials can be used for electric power generation and refrigeration[2].

In 1822, Thomas Johann Seebeck[1, 3] discovered that a close loop with two different conductors would deflect a compass needle when one junction of the two conductors was heated. Seebeck falsely concluded this phenomenon as a magnetic effect. Later it was proved that a current was generated when one hetero junction of the closed loop was

heated and the current developed a magnetic field. This effect is called Seebeck Effect, demonstrated in Fig 1.1. Nevertheless, he worked on this effect and tested a great number of different materials including metals, semiconductors, etc... He introduced the Seebeck coefficient α to rank the materials Seebeck effect property. The Seebeck coefficient is defined as:

$$\alpha = -\frac{\Delta V}{\Delta T}. \tag{1.1}$$

Equation (1.1) can be written as

$$\alpha = \frac{8\pi^2 k_B^2}{3eh^2} m^* T \left(\frac{\pi}{3n}\right)^{\frac{2}{3}}, \tag{1.2}$$

where k_B is Boltzmann Constant, e is elementary charge, h is Planck Constant, m* is the carrier's density of state (DOS) effective mass, T is temperature and n is the carrier concentration.

In addition, the merit of thermoelectric zT is defined as[4]:

$$zT=\alpha^2\sigma T/K, \tag{1.3}$$

where σ is the electrical conductivity and k is the total thermal conductivity. The total thermal conductivity includes lattice thermal conductivity (K_L) and electronic thermal conductivity (K_e), which can be written as:

$$K = K_L + K_e \tag{1.4}$$

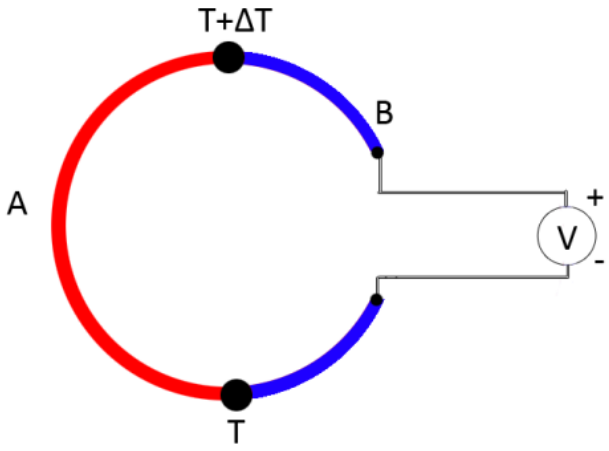

Fig 1.1 Schematic for Seebeck effect, A and B are two different conductive materials. When one junction of A and B is heated, a current will be generated.

1.3. Peltier Effect

In 1934, Jean Charles Athanase Peltier[1, 5] discovered an inverse effect. He observed that when a current passed a loop formed by several different conductors, the temperature of the vicinity of the hetero junctions would change. Heat will be generated at the first hetero junction, absorbed at the second hetero junction, as Fig 1.2 shows. This effect is now used for cooling systems, which can pump the heat from cold side to hot side. Compared with traditional cooling system it has the merit of long lifetime, small, environmental friendly and so forth, while it is too inefficient for most applications[6].

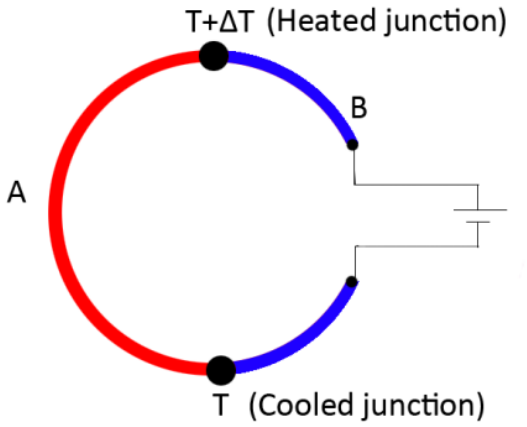

Fig 1.2 Schematic for Peltier effect, A and B are two different conductive materials and form a close loop. When a power applied on this loop, one junction of A and B will be heated while the other one will be cooled.

1.4. Thomason Effect

The Seebeck Effect and Peltier Effect both describe the thermoelectric effects in hetero junctions, while in 1851 William Thomson (Lord Kelvin) predicted the third thermoelectric effect, Thomson Effect[1, 7]. It describes the thermoelectric effect in homogeneous materials and was observed by him subsequently. The Thomson Effect is that when a current passes a homogeneous conductor or semiconductor (except superconductor) under a temperature gradient, heat will be either emitted or absorbed. The heat can be calculated with equation below[1]:

$$q = \rho J^2 - \mu J \frac{dT}{dx} \tag{1.5}$$

where ρ is electrical resistivity, J is current density and μ is Thomson Coefficient. μ is defined as[1]:

$$\mu = T\frac{d\alpha}{dx} \tag{1.6}$$

μ can be either positive or negative, depends on different materials. For instance, when a current passes a material from the hot side to the cold side, as figure 1.3 shows, the material will emit heat if it has a positive μ while it will absorb heat if its μ is negative. Complementarily, a temperature gradient applied on a homogeneous conductor or semiconductor will cause an electric voltage difference along the temperature gradient.

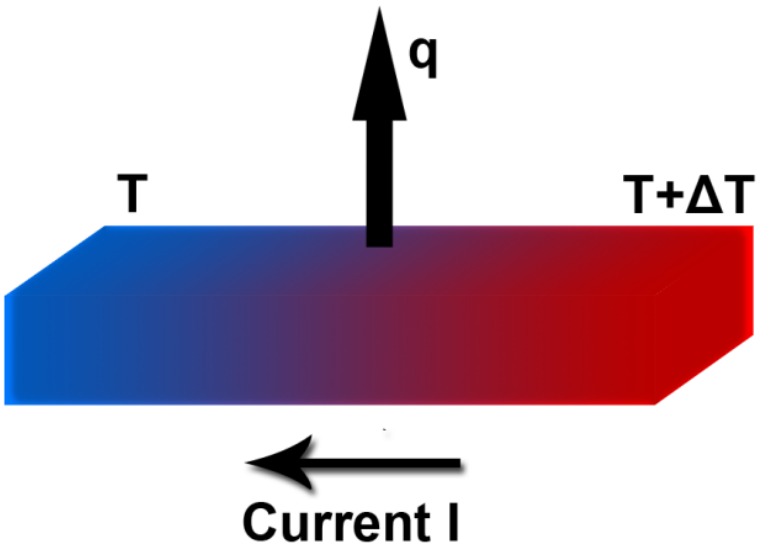

Figure 1.3 Schematic of Thomason effect. When a current passes from the hot side to the cold side of an homogenous conductive materials, heat besides Joule heat will be either absorbed or emitted depends on different materials.

1.5. Conflicting Characteristics of Thermoelectric Materials

Since thermoelectric effects' discovery, a great number of materials including metals and semiconductors have been used to make thermoelectric devices. Fig 1.4 illustrates the principles of thermal power generation and refrigeration devices. The merit of thermoelectric at room temperature (300K) reached 1 about half a century ago. Nevertheless, the progress in the merit is very modest in the past several decades. The reason for the low efficiency of thermoelectric is that a high merit requires an optimization of a combination of conflicting material characteristics, including thermal conductivity, electrical conductivity, etc. Since 1990s L.D. Hicks began to work on nanostructure materials for thermoelectric devices and achieved great progress[8-11]. However the efficiency is still far from practical applications.

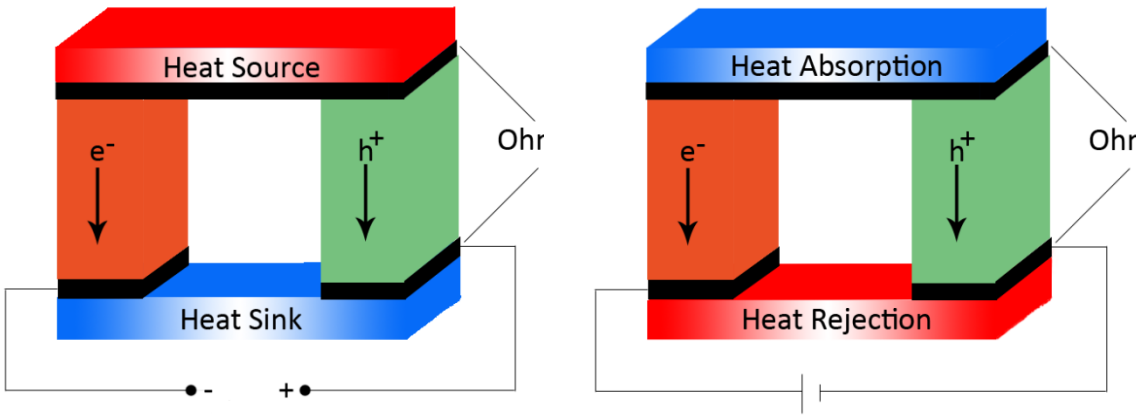

(a) (b)

Fig 1.4 Schematic of thermoelectric devices (a) power generation mode (b) refrigeration mode

According to the equation 1.2 and 1.3, the merit of thermoelectric zT is related to the electrical conductivity and total thermal conductivity. A high zT requires high electrical conductivity and low total thermal conductivity. Electricity is carried by electrons in metals while by holes and electrons in semiconductors; Heat is carried by phonons and electrons. As the equation 1.4 shows the total thermal conductivity includes lattice thermal conductivity and electronic thermal conductivity. The electronic thermal conductivity can be expressed as[12]

$$K_e=L\sigma T, \qquad (1.7)$$

where L is Lorenz number, which is a constant. According to equation 3.1, the electronic thermal conductivity is proportional to the electrical conductivity when temperature keeps the same. This is the first conflict when improving the thermoelectric merits.

As the conflicts between σ and K_e, reducing K_l is a key to obtaining a high zT. Here we introduce a ratio[13]

$$r = \frac{K_e}{K_e+K_l} \qquad (1.8)$$

Substituting the equation 1.8 and 1.4 in equation 1.3, we can get a linear relationship between zT and r

$$zT = r\alpha^2/L \qquad (1.9)$$

Substituting α with equation 2.2, equation 3.3 can be written as

$$zT=\frac{64{k_B}^4 {m^*}^2(\frac{1}{n})^{4/3}\pi^{16/3}rT^2}{273^{1/3}h^4Lq^2} \qquad (1.10)$$

Replace product of all the constants in equation 3.4, a relationship between ZT and r, effective mass, carrier concentration is obtained as:

$$zT \sim r m^{*2} T^2 \left(\frac{1}{n}\right)^{4/3} \qquad (1.11)$$

Therefore, to get a high zT, a high carriers' DOS effective mass m* and a low carrier concentration n are required[14, 15]. However, a large m* leads a low μ, while a low μ and a low n lead a low σ, which finally results in a small r. As a result, zT is a combination of conflicting properties.

1.6. Nanocrystals for Thermoelectric Devices

Before 1990s, thermoelectric researches focused on bulk materials. At that time, nanomaterials were regarded as low efficiency materials for thermoelectric, since the electrical conductivities in the nanocrystals are very low. In 1957, A.F. Ioffe introduced the narrow band gap theory for thermoelectric[16], which described that zT could be maximized in narrow band-gap semiconductors. Later on most research work on thermoelectric was based on Ioffe's theory, including Bi_2Te_3[17, 18], PbTe[19-21] and Si-Ge[22, 23] alloys. The main methods to improve the merit of thermoelectric in bulk materials were doping, alloying, micro-compositions, etc., whereas due to the limitations of bulk materials, the zT value did not exceed 1.0.

After 1990s, L.D. Hicks introduced the idea that the thermoelectric efficiency can be highly promoted in low dimensional materials[8-10]. One reason is that the DOS near Fermi level (E_F) could be adjusted and increased in low dimensional materials. DOS can be expressed as:

$$g(E) = \frac{d\Omega(E)}{dE} = \frac{8\pi\sqrt{2}}{h^3} m^{*3/2} \sqrt{E - E_c}, \qquad (1.12)$$

where Ω(E) is the number of states of electrons, E is the energy electrons and E_c is the bottom energy of conductive band. E can be expressed as:

$$E = \frac{\hbar^2 k^2}{2m^*}, \qquad (1.13)$$

where ħ is reduced Plunk constant, k the wave number of electrons or holes. The Ω(E) has different expressions for different dimensional materials as equation 1.14-1.16 show.

3D: $\Omega(E) = \frac{4\pi}{3} k^3$, (1.14)

2D: $\Omega(E) = k^2$, (1.15)

1D: $\Omega(E) = 2k$, (1.16)

And in 0D materials (quantum dots), the energies of electrons and holes are all quantized. As a result, the states only exist on allowed energy levels. According to equation 1.12 to 1.16, we can get the conclusions below:

3D: g(E) ~ $\sqrt{E}$

2D: g(E) is a constant and does not change with E.

1D: g(E) ~ $1/\sqrt{E}$

In low dimensional materials, due to the barriers at the boundaries, electrons with energies lower than the barriers are confined to the nanocrystals, while electrons with energies higher than the barrier are able to transit to the higher energy level, where

electrons can transport though boundaries. In other words, the g(E) is not continuous in low dimensional materials. Figure 1.5 is a schematic of the relationship between DOS and energies in different dimensional materials. Since low energy electrons are filtered by boundary barriers in low dimensional materials, the DOS of electron is promoted. According to equation 1.12, m^* is increasing with g(E), so m^* in low dimensional materials is larger than in bulk materials. A larger m^* will lead a large α according to equation 1.2. Finally a proper E_F, which can determine g(E), is able to maximize the merit of thermoelectric. The value of E_F which maximizes zT is probably different from the one that maximize m^* or α[24].

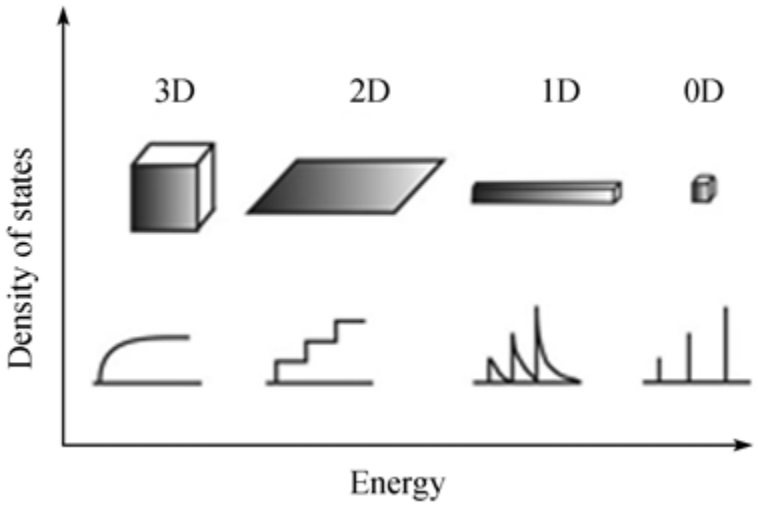

Fig. 1.5 Schematic of Electron density of states vs electron energy for different dimensional materials

At the same time, the abundant boundaries in low dimensional materials will increase the scattering of phonons and reduce the lattice thermal conductivity. Equation 1.17 shows the relationship between phonon scattering and lattice thermal conductivity.

$$K_l=\frac{1}{3}Cvl \quad (1.17)$$

C is the heat capacity; v is the phonon velocity; l is the mean free path of phonons, which is defined as the mean distance that a phonon can move between two collisions. l decreases when scattering of phonons increases. Finally, K_l drops in low dimensional materials. In sum, the thermoelectric efficiency can be promoted by reducing the dimensions of materials.

Later in 1990s, G.A. Slack introduced a theory called Phonon Glass Electron Crystal (PGEC)[25]. In this theory, he suggested to design some thermoelectric materials that behavior like crystals when transporting electrons while like glasses when transporting phonons. Based on this theory, some nanomaterials with special structures are studied, like skutterudite[14, 26-31], Clathrate[32-34] materials etc. Up to today, many experimental results[35-53] show that zT are improved in nanostructured materials, which support the low-dimension thermoelectric theory.

1.7. Research Goals

Bismuth (Bi) is an important constituent element used for thermoelectric. Not only the metallic bismuth can be used as thermoelectric materials, since its thermal conductivity is the second lowest in metals[54], but also it can form a great number of compounds used for

thermoelectric devices, including Bi-Te system, Bi-Se system, (Bi, Sb)-(Te, Se) system, etc. After all, Bi is one of the most valuable elements for thermoelectric devices.

My research work focuses on bismuth nanoparticles synthesis and thermoelectric characteristics tests. I will try to make bismuth nanoparticles in uniform sizes and shapes. After obtaining the uniform Bi nanoparticles, I will make them into thick films and tested the electrical conductivity and thermal conductivity. Besides, I will make another batch of Bi thick films with commercial Bi powders. The differences in thermoelectric characteristics between the two Bi particles of different scales will be investigated.

Chapter 2. Experimental Techniques

2.1. Synthesis

Nanomaterials synthesis methods can be divided into physical methods, like physical vapor deposition (PVD), mechanical milling and chemical methods, like chemical vapor deposition (CVD), hydrothermal reaction, liquid phase reaction and microemulsion method. In my research work, I focused on hydrothermal reaction and liquid phase reaction.

2.1.1. Hydrothermal Reactions

Hydrothermal synthesis is a technique of crystalizing materials in aqueous under high pressure and temperature. It originates from the hydrothermal circulation which describes the hot water circulation within the Earth's crust. Hydrothermal synthesis was first reported by German chemist R. Bunsen in 1839[55]. He obtained barium carbonate and strontium carbonate by heating precursor aqueous above 200℃ and $1 * 10^7$ Pa in a thick-wall glass container.

Later on, hydrothermal reaction was improved both in reaction equipment and procedure. Today hydrothermal reactions usually react in an autoclave, which is resistant to high temperature and pressure. Figure 2.1 is a schematic of hydrothermal reaction. The principle of the hydrothermal reaction is that the high temperature and pressure during the reaction increase the solubility of the product. When the concentration of the product reaches saturation, it will precipitate and crystalize. By changing the reaction conditions, like time, temperature, pH value etc., different products may be obtained. For instance, for the same precursor bismuth hydroxide and iron hydroxide reacting under different

hydrothermal conditions, only the reaction with a temperature of 200℃ and the presence of 4 M KOH will get the pure $BiFeO_3$, while hydrothermal reactions with other conditions will generate some impurity phases like $Bi_2Fe_4O_9$ and $Bi_{25}FeO_{40}$[56]. Besides, the hydrothermal conditions will greatly impact the morphology of products. With a proper hydrothermal procedure, low dimensional materials can be obtained. In addition, due to the high temperature and pressure, the solubility of precursors will increase as well. Thus hydrothermal methods sometime can accelerate a reaction.

As the merits of the hydrothermal reaction mentioned above, it is now widely used for synthesis nanocrystals. In my work, I used a Teflon container sealed in a stainless autoclave. Figure 2.2 is the image of my autoclave.

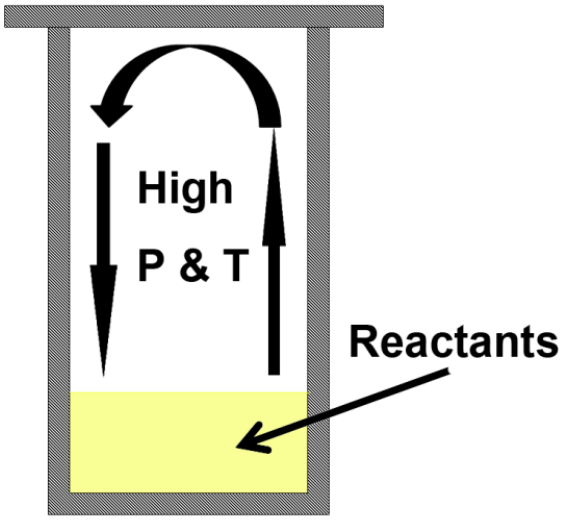

Fig. 2.1 Schematic of hydrothermal reaction

Fig 2.2. the stainless steel autoclave and Teflon container used for hydrothermal reactions.

2.1.2. Liquid Phase Reactions

Liquid phase reaction is another common method for nanocrystals synthesis. Its mechanism is that all the precursors are dissolved in solvent while the product is insoluble in the solvent. When heat the precursor solution, the reaction happens and the products precipitate. Figure 2.3 is a schematic of liquid phase reaction with water condensation. As this schematic showing, the reactants are under magnetic stirring during the whole reaction procedure in order to keep reaction condition uniform. A condenser is added to the equipment for reflux, where the vapor of solvent gets cooled and drops back

to the flask. Usually argon protections are applied during the reactions in order to prevent the products from getting oxidized.

Figure 2.4 is the image of my liquid phase reaction system. The precursors react a three-mouth flask. The flask is heated by a heat mantle and the temperature of the reaction is measure by a thermocouple. Both of them are connected to a temperature controller, which keeps the reaction temperature constant.

To synthesis nanocrystals with liquid phase reactions, ligands are needed to reduce the surface energies of nanocrystals, otherwise the nanocrystals will aggregate due to the high surface energies. In my work, I used oleic acid as ligand. Also I used a PAA-PS diblock copolymer to control the morphology of my Bi nanoparticles. The PS block in the template work as a ligand. More details about the mechanism of ligands will be discussed in later chapters.

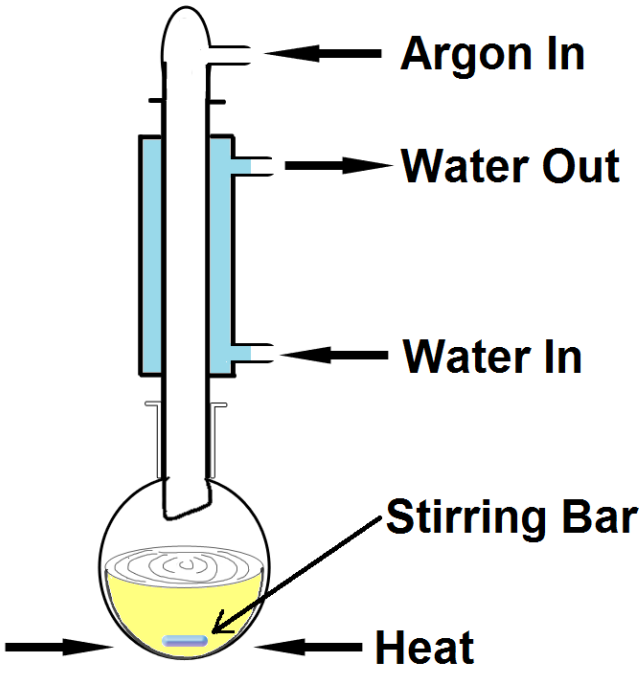

Fig. 2.3 Schematic of liquid phase reaction cooled by water condensation

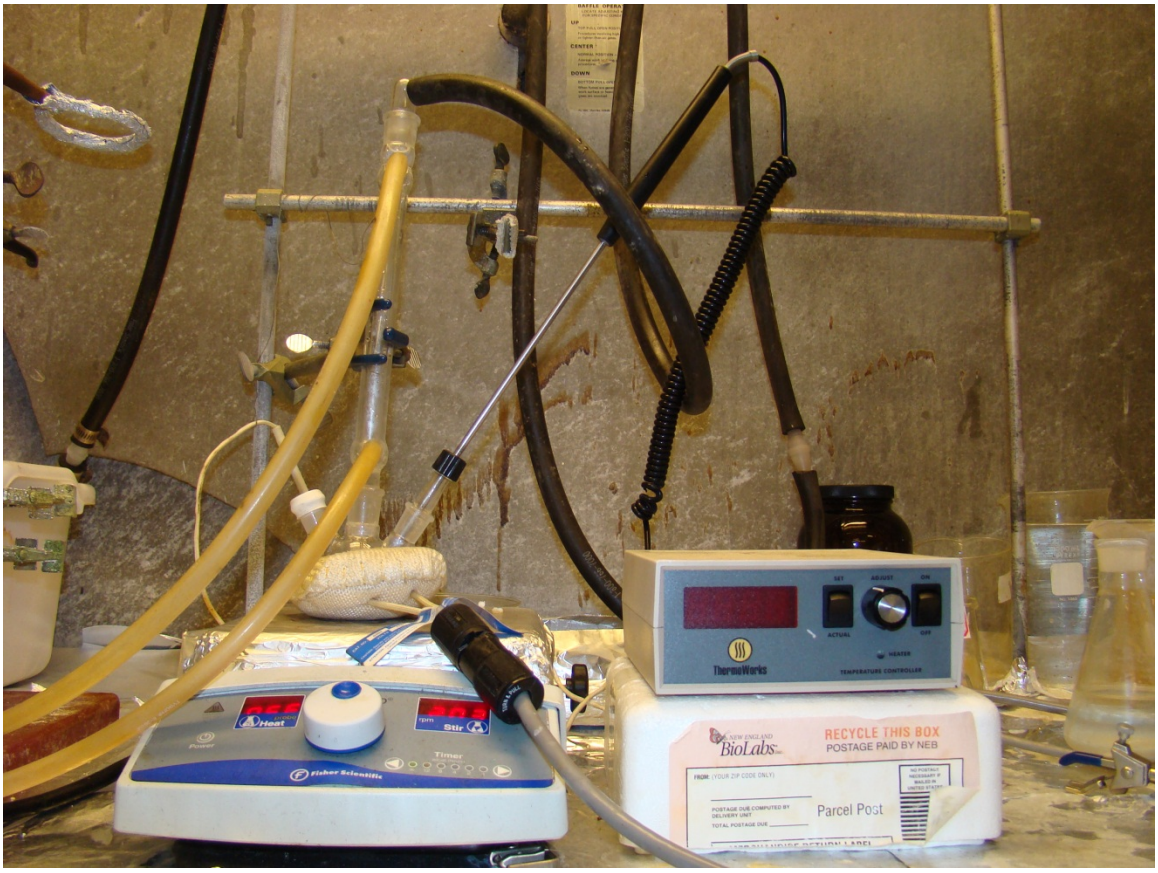

Fig 2.4. liquid phase reaction set with reflux.

2.2. Purification

According to thermal dynamics, most chemical reactions are under a thermal dynamic balance, which means precursors cannot get fully reacted. As a result, the outcome of a reaction is a mixture of the products, reactants and some residual solvent. Sometimes byproducts are generated and mixture with the products. Thus purification is a very important step to obtain pure products. In nanocrystals synthesis, purification has another important effect – obtaining nanocrystals with a uniform size and shape, because the unpurified nanocrystals usually have a certain range of size dispersion and the shape of them may vary as well.

In my experiments, I used a centrifuge to wash my products with different dispersant and precipitant. In order the get pure and size-uniform nanocrystals, all the unreacted precursors and smaller or larger particles should be removed. The strategy of purification is that the dispersant should dissolve the precursor and solvent and make the nanocrystals well dispersed in it while the precipitant should dissolve the precursor and solvent as well, but make the nanocrystals precipitate. As a result, using a proper dispersant and precipitant, all of the unwanted substance can be well removed and different sizes of nanocrystals can be obtained by changing the ratio of dispersant and precipitant and by adjusting the speed and time of centrifuge. Figure 2.5 is the image of the centrifuge and centrifuge tubes I used for my Bi nanoparticles purification. It has a maximum speed of 6.5 k rpm.

2.3. XRD

X-ray diffraction (XRD) is a most common method for phase analysis, which is based on the elastic scattering of X-ray. It is an application of Bragg's law[57], which is expressed as:

$$n\lambda = 2d\sin\theta, \qquad (2.1)$$

where n is an integer, λ is the wavelength of the X-ray, d is the spacing between planes in crystals and θ is the half scattering angle. Figure 2.6 shows the mechanism of Bragg's law. The incident X-ray scatters at every hkl plane and the lower beam travels a length of $2d\sin\theta$ more than the upper beams. When the Bragg's law is satisfied, which mean the

extra distance travelled by the lower beam is exactly the integral multiple of λ. As a result, these two X-ray beams superpose and the intensity of X-ray beams scattered at this angle is higher than that at other angles, which do not meet Bragg's law. In an actual crystal, there are more parallel planes and more scattered X-ray beams will superpose at Bragg diffraction angle and the intensity will be much higher than that at other angle. The XRD equipment uses a detector to collect all the scattered X-ray beams and outputs an pattern of the intensity. Peaks occur at the Bragg diffraction angles. By comparing the XRD pattern with the standard XRD pattern, we can determine the structure of the crystals.

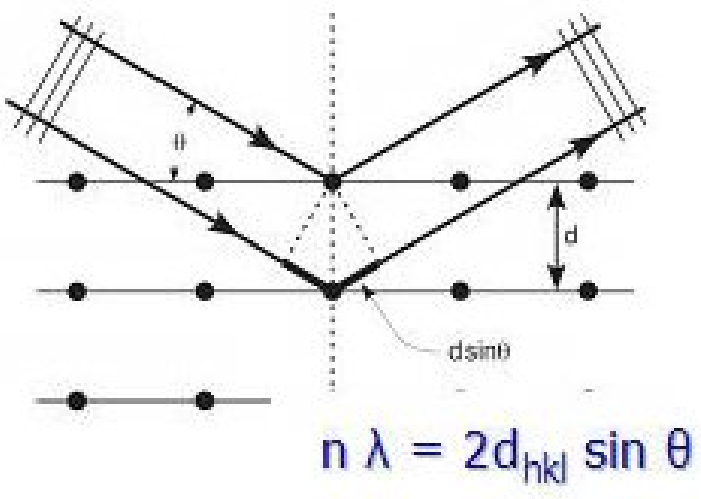

Fig. 2.6 the mechanism of Bragg's law

In my experiments, I used a Scintag Powder X-Ray diffract machine to determine the phase my nanocrystals. The voltage and current. The incident ray is Cu K-α X-ray, whose wavelength is 1.5418Å. The standard XRD patterns are obtained by International Centre for Diffraction Data. Figure 2.7 is the image of the XRD machine used in my work.

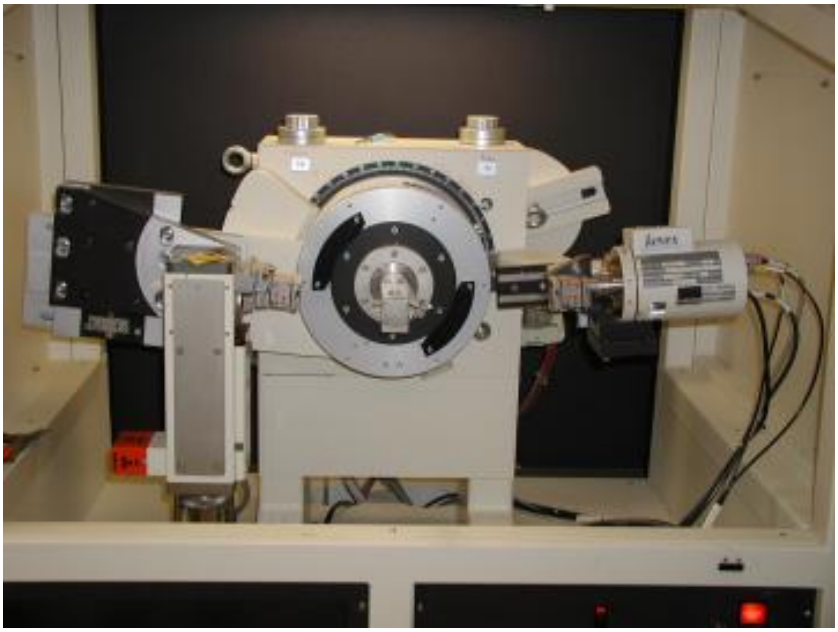

Fig 2.7 Scintag Powder X-Ray machine purchased by Iowa State University in 1991 and a new X-ray generator installed in 2002, which provides more reliable incident X-rays.

2.4. SEM

Scanning electron microscope (SEM) is usually used for observing nano or microstructures. The image is obtained by scan the sample with an electron beam of high energy. To ensure the scanning of electron beam, it requires the surface of the sample conductive. The one I used is a FEI Quanta-250 SEM operated at 20 kV under high vacuum. It is equipped with a field-emission gun which can provide a resolution of 1.2nm.

Fig. 2.8 The FEI Quanta-250 SEM used for examining the morphology of Bi nanoparticles.

2.5. TEM

Transmission electron microscopy (TEM) is another kind of electron microscopy, which is used for investigating the size and structure of nanocrystals. It usually has higher resolution than SEM. In addition, the requirement of surface conductivity of SEM causes extensive sample preparation, and sometimes it even limits the usage of SEM, while

TEM can observe samples, which are insulate. Due to the benefits of TEM, it is more widely used for observing nanostructures.

In my research, I used a JEOL 2100 scanning transmission electron microscope (STEM) operated at 200kV to image. A typical TEM sample preparation for my Bi nanoparticles is dispersing the Bi nanoparticles in toluene, diluting it to a proper concentration and dropping the solution on a TEM grid. The TEM grids are 400 mesh copper grid coated with carbon (CF400H-Cu 400 mesh, purchased from Electron Microscopy Science). More details about the parameters of the TEM sample solutions will be discussed in later chapters.

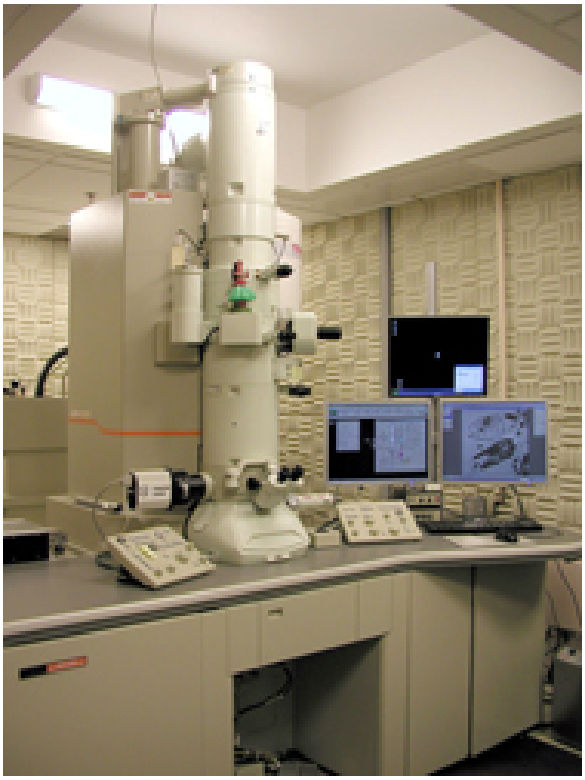

Fig 2.9. The JEOL 2100 STEM used for observing the morphologies of bismuth nanoparticles.

2.6. Spin Coating

Spin coating is usually used for fabricating uniform thin films on flat substrates, like glass slides or silicon wafers. A typical spin coating process is that an excessive amount of suspension or solution containing the film components is dropped on the substrate which is mounted on the spin coating machine by vacuum and the substrate is rotated at a high speed for a certain time. Due to the centrifuge force, the drop will be spread and thrown out of the substrate. Only a thin layer of the solution or suspension will be left on the substrate forming a uniform thin film. The speed and time impact the thickness, uniformity and some other properties of the spin coating thin films. I used a ..spin coating machine.

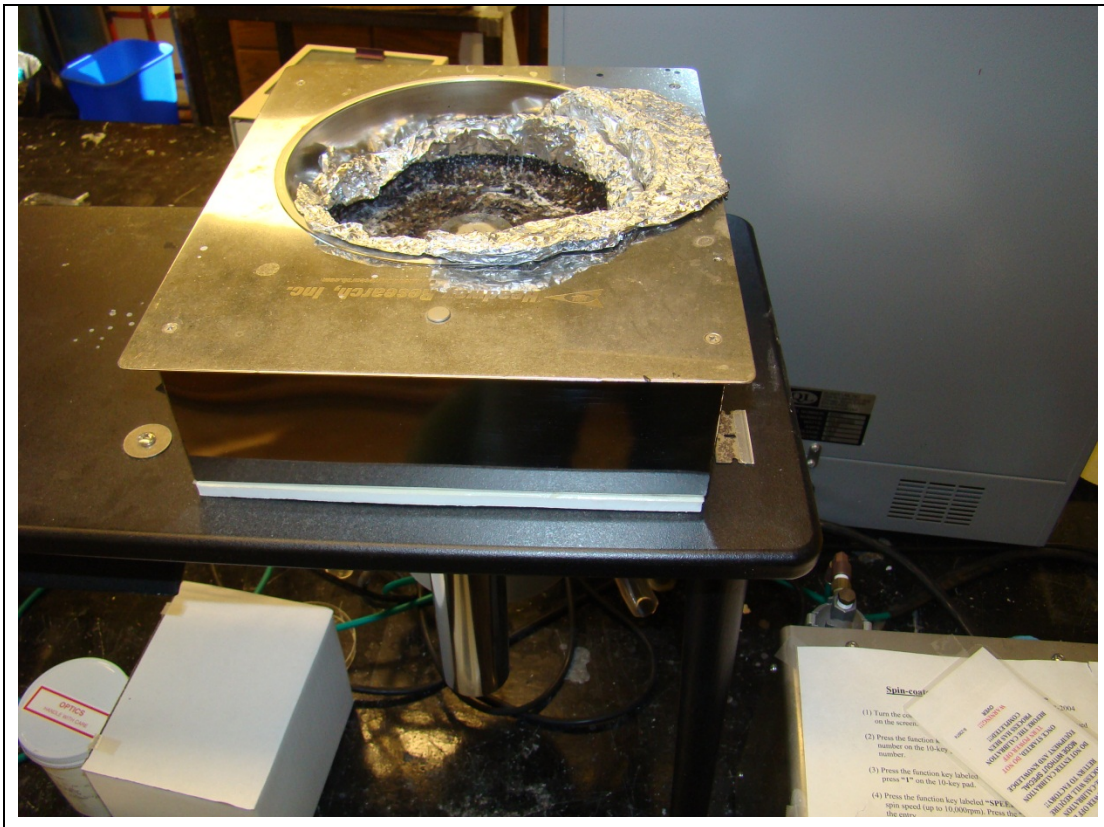

Fig 2.10. Spin coating machine used for thin film fabrtication.

2.7. Hot Press

Hot Pressing is the common method to make thick films. It applies a high pressure when heating the sample powders to a high temperature for several minutes. During the procedure, the powders are sintered and form a thick film. I used a Carver 3895 automatic presses set with a half-inch die to perform the hot pressing. The process of hot press is that the half-inch die with sample powders filled inside was placed between the clamps of the hot press set and a set pressure was applied on the die for 5 minutes after it was heated to a certain temperautre.

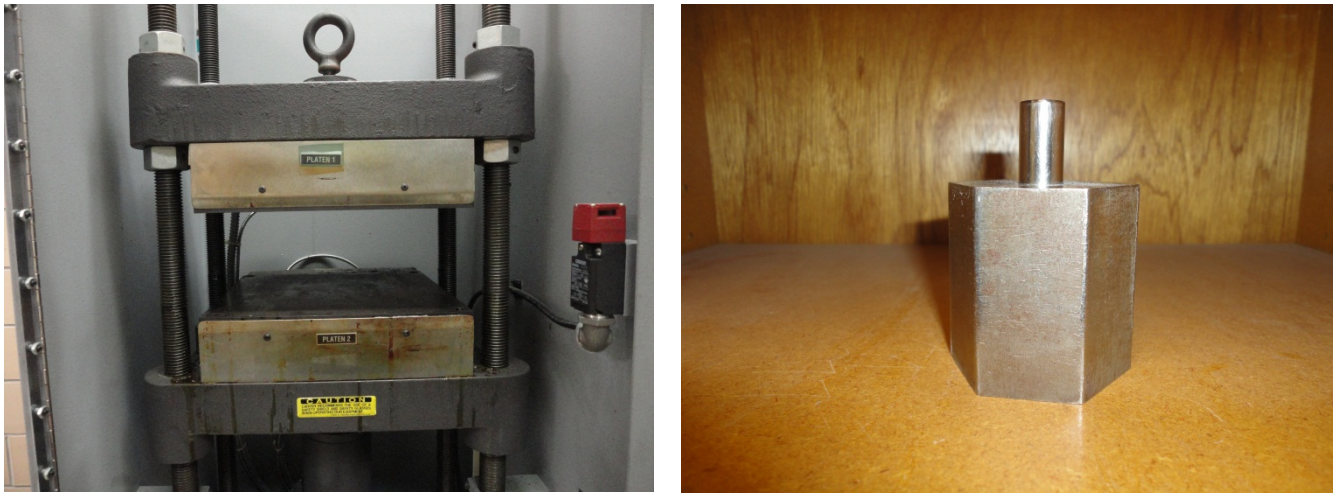

(a) (b)

Fig 2.8 (a) the hot press set used for making disks with powder samples, (b) the half-inch die used for hot press process.

2.8. TGA

Thermo gravimetric analysis (TGA) is a kind of testing method for material characterization. It can determine the degradation, oxidation or some other reaction temperature of a certain substance by measuring the change weight of a sample related to

the change of temperature. In my research, I used a TA Q50 TGA machine to measure the oxidation and degradation temperatures of my samples.

Fig . the TA Q50 TGA used for testing the oxidation and degradation temperature of materials.

2.9. Four-Point Probe Measurement

Four-point probe measurement is used for testing the electrical conductivity of films. The resistance of a material is related to its resistivity (ρ) and shape, which can be written as:

$$R = \frac{\rho l}{A}$$

here l is the length of a material and A is the area of the cross-section through which the current flows. When we use 2-point probe measurement to test the electrical conductivity, the contact resistance between the probe and the material would disturb the result. The four-point probe measurement can well solve this problem, since the voltage applied and measured from different points and the resistance of the voltage meter can be regarded as infinite, so the detected voltage can be regarded as the voltage on the tested materials between the second and third point. In my research, I used a Jandel RM2 four-point probe measurement to test the electrical conductivities of samples.

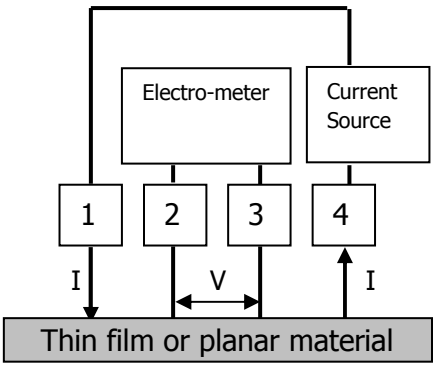

Fig. 2.11 A schematic of 4-point probe measurement.

Fig. the four-point probe measurement used for testing the electrical conductivity of thin films.

Chapter 3. Bismuth Nanoparticles Synthesis by Hydrothermal Reactions

3.1. Hydrothermal reactions without any surfactant

As mentioned in Chapter Two, the hydrothermal reactions were performed in a Teflon container sealed in a stainless autoclave. The precursor was bismuth (III) nitrate pentahydrate ($Bi(NO_3)_3 \cdot 5H_2O$, 99.999%, Sigma-Aldrich). 339.5 mg precursor was dissolved in 10 ml Dimethylformamide (DMF) under magnetic stirring. DMF is not a good solvent for bismuth nitrate. Even after being stirred for 10 hours, the bismuth nitrate was still partially dissolved in DMF and a suspension was formed. Nevertheless, the high pressure and temperature during the hydrothermal procedure would increase the solubility of bismuth nitrate in DMF. The mixture of bismuth nitrate and DMF was transferred to a Teflon container and sealed with a stainless autoclave, which was heated in an oven at 120 ℃ for 12 hours.

After the reaction, the products were collected in the bottom of the Teflon container, which were grey powders. The products were dispersed in 8 ml toluene in a 15 ml polypropylene centrifuge tube (Corning) and shaken for 1 minute. 4 ml ethanol was added to the suspension and shaken for another 1 minute. Then the centrifuge tube was placed in a VWR centrifuge machine and centrifuged at 3.6k rpm for 5 minutes. Same centrifugation process was repeated for 2 more times.

After centrifuge, the products were dried in an oven at 80℃ under low vacuum. The components of the products was characterized by the Scintag Powder X-Ray diffract

machine operated at 40 kV and 30mA. Figure 3.1 is the XRD result of the products. The peaks fit the standard XRD pattern of bismuth as shown in Fig. 3.2, which means the products were pure metallic bismuth.

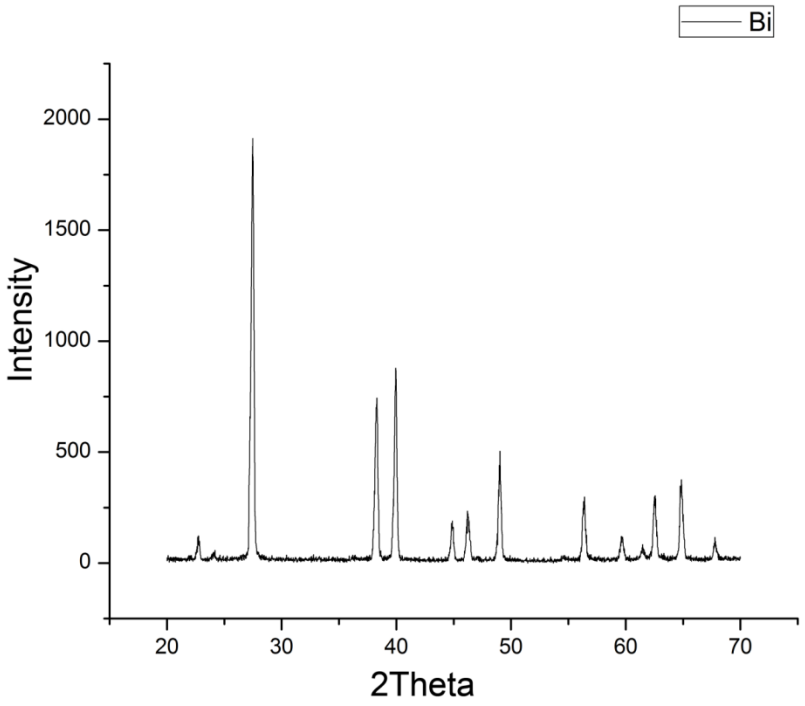

Fig. 3.1 XRD result of Bi particles synthesized by hydrothermal reaction without ligands.

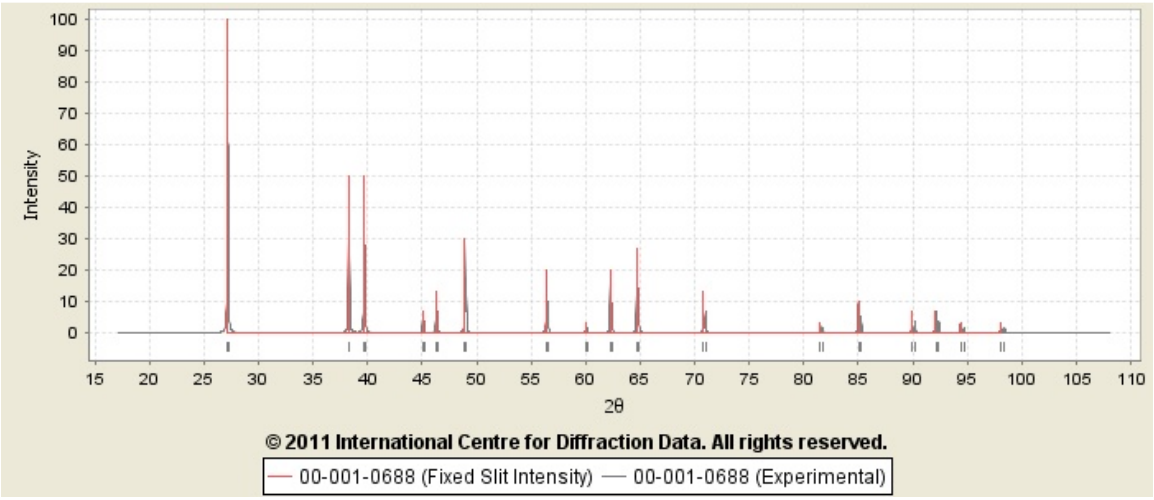

Fig. 3.2 Standard XRD result of metallic bismuth provided by International Centre for Diffraction Data.

The morphology of the bismuth particles was characterized by the FEI Quanta-250 SEM operated at 20 kV under high vacuum. Figure 3.3 is the SEM image of the bismuth particles. The SEM image shows that the morphology of bismuth particles is not uniform. The dispersion of particle sizes is too large; the particle sizes range from 20µm to 40µm; the shapes of the particles are not uniform and the surfaces of the particles are rough.

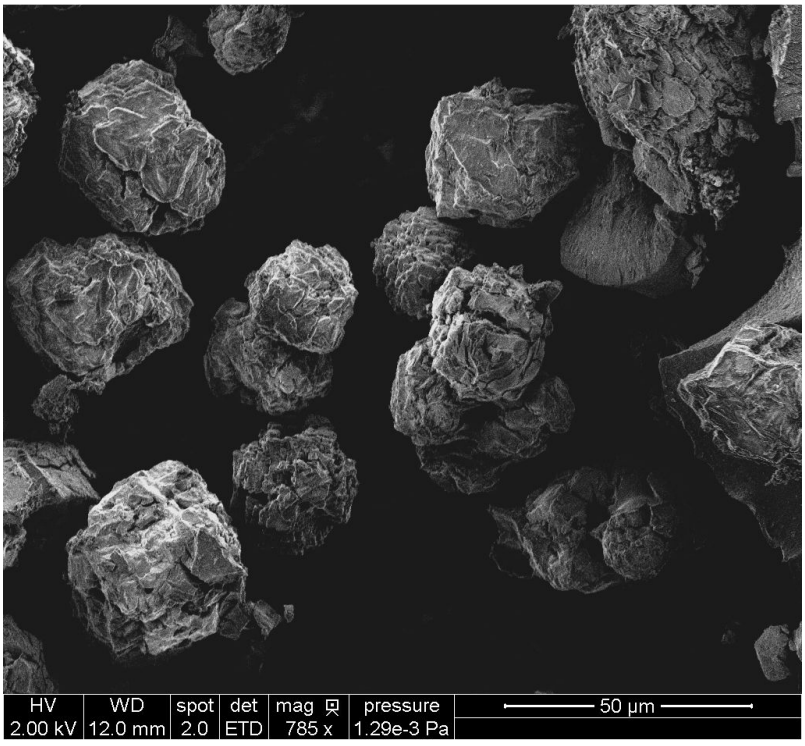

Fig. 3.3 Morphology of bismuth particles synthesized by hydrothermal reaction without ligands.

3.2. Hydrothermal reaction with the help of ligands

The morphology of bismuth particles synthesized by hydrothermal without ligands was out of control. In order to obtaining bismuth nanoparticles with more uniform morphologies, I added ligands in the previous hydrothermal process.

Ligands can be polymers or monomers, which contains some functional groups, like carboxyl, hydroxyl, etc. Due to the functional groups, the ligands will attach to the nanocrystals during the growth and form some coordination complex. As a result, the further growth of the nanocrystals is prevented by the ligands. Moreover the surface energies of the nanocrystals are lowered since they are covered with ligands and the aggregations of nanocrystals are prevented as well. With the presence of ligands in synthesis process, the morphologies of nanocrystals can be better controlled[58]. In addition, ligands are often used for making nanorods[59], nanowires[60] and some other nanostructed[49, 61] crystals, because some nanocrystals are anisotropy, which means the ligands prefer to attach to some of their crystalline planes, while the direction without ligands could grow freely[62].

I used oleic acid as ligands to control the morphologies bismuth nanocrystals in the hydrothermal process. The formula of oleic acid is $CH_3(CH_2)_7CH=CH(CH_2)_7COOH$, which has two isomers. Fig 3.5 shows the structures of the two isomers of oleic acid. Oleic acid only has one hydroxyl functional group at one side of its chain and this hydroxyl functional group enables an oleic acid monomer to attach to the nanocrystals, while it does not have any functional group on the other side or along the chain, so it will

not sticky to another oleic acid monomer. Therefore oleic acid is a very good ligand for nanocrystals synthesis.

The hydrothermal process is the same as the previous one except for adding 1 ml oleic acid as ligands. The purification process was the same as previous one as well. Fig 3.5 is the XRD result of the bismuth particles. In this XRD result, the peaks are broader than that in Fig. 3.1. This result could be explained by Scherrer equation[63] , which is

$$D = \frac{K\lambda}{\beta \cos\theta} \quad , \qquad (3.1)$$

where D is crystalline size, K is Scherrer constant, λ is X-ray wavelength, β is the full width at half maximum (FWHM) and θ is diffraction angle. According to the equation 3.1, β is inverse proportional to the crystalline size. In other words, the peaks of XRD would broaden when the crystalline size decreases. Thus the broad peaks in the XRD result indicated the nanoscale size of the bismuth particles. In addition, the intensity of the diffracted X-ray is much lower than that of the previous bismuth particles. This is because there are less crystalline planes in nanocrystals than in microcrystals, so less X-ray would be reflected by a certain group of crystalline planes.

Fig. 3.7 is the TEM images of the bismuth nanoparticles synthesized by hydrothermal with oleic acid as ligands. The TEM images show that the sizes of bismuth particles are all less than 50 nm, which are much smaller than the bismuth particles synthesized by the previous hydrothermal process. Also the shapes of the Bi particles are almost cubic. Therefore the oleic acid controlled the morphology of bismuth particles during the hydrothermal process. However, the dispersion of the particles size is not uniforms,

ranging from 15 to30 nm. In addition, Fig 3.7 (a) and (b) show that there were some other substance in the TEM images beside the bismuth nanoparticles. This substance is probably the amorphous precursor, which cannot be detected by XRD.

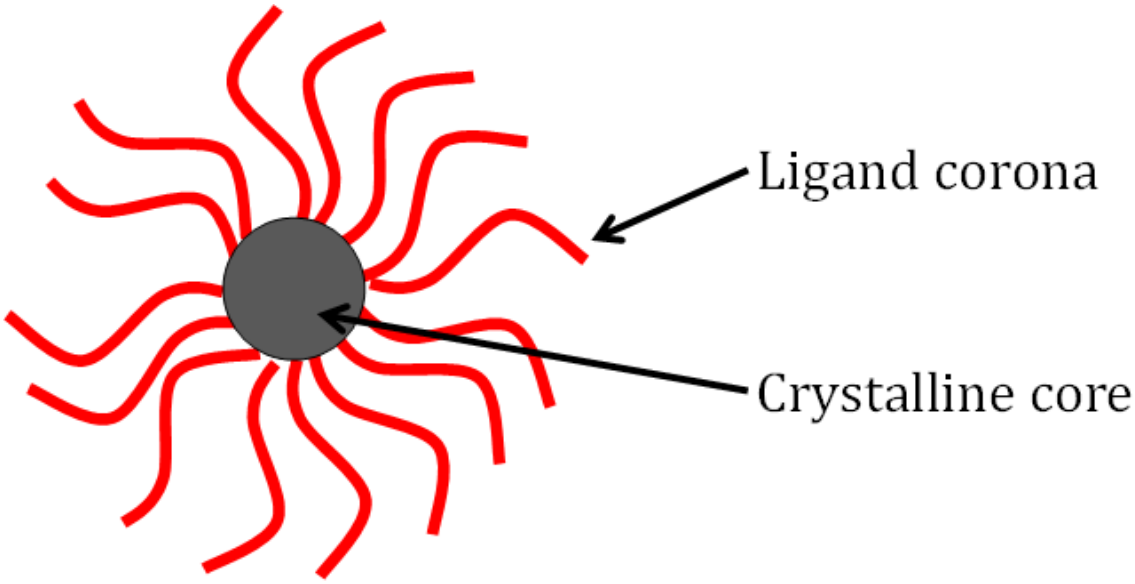

Fig. 3.4 A schematic of the mechanism of ligands. When the ligands attached to the crystals the growth of the crystals would be decelerated and eventually stopped.

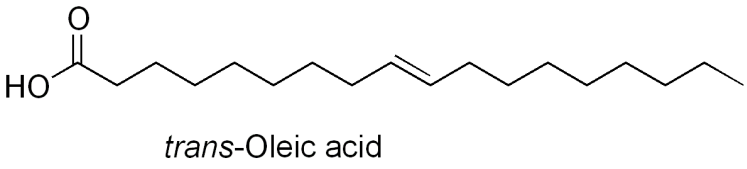

trans-Oleic acid

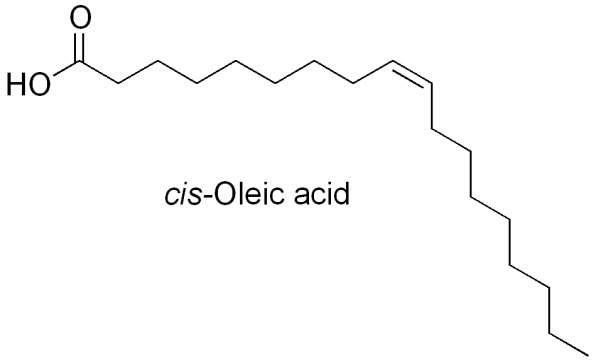

cis-Oleic acid

Fig. 3.5 The structures of two isomers of oleic acid. Both of them has one hydroxyl which makes them able to attach to the nanocrystals.

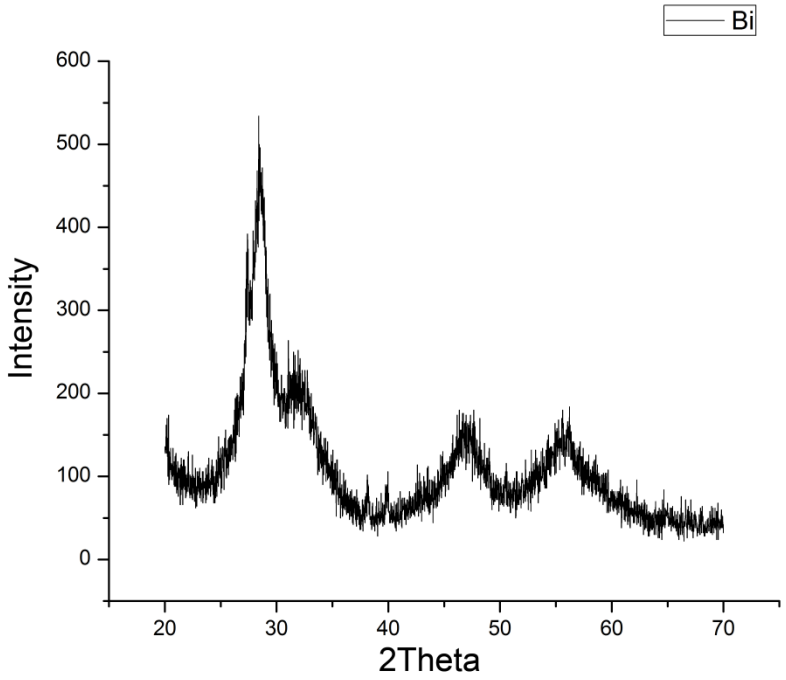

Fig. 3.6 XRD result of the bismuth particles synthesized by hydrothermal with oleic acid as ligand.

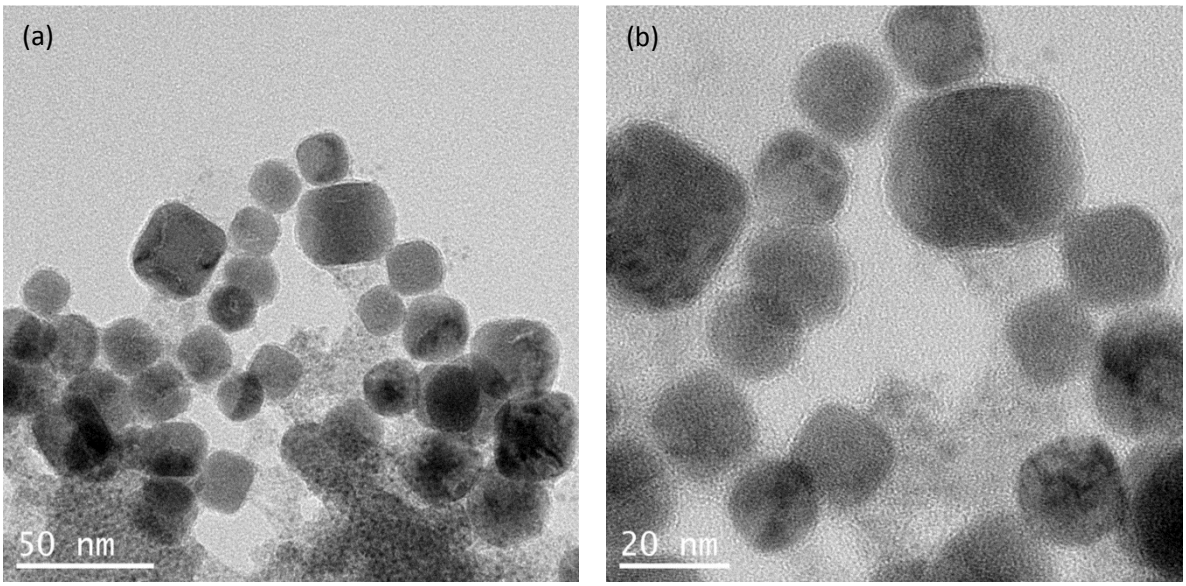

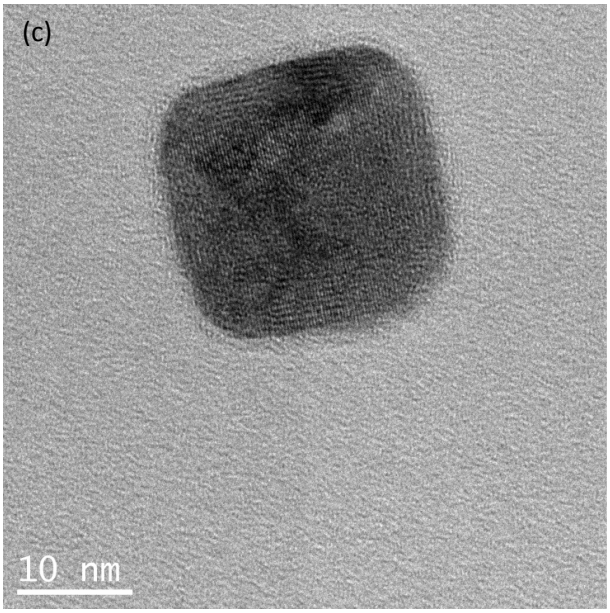

Fig. 3.7 TEM images of the bismuth particles synthesized by hydrothermal with oleic acid as ligand.

3.3. Results and discussions

The hydrothermal process without any ligands would generate bismuth micro particles with different shapes and wide size distribution. Hydrothermal reaction with oleic acid as ligand is a possible method to synthesize bismuth nanoparticles. The particle sizes can be controlled in nanoscale and the shapes of particles are almost uniform. However the sizes are still not uniform, because the conditions of the reaction are difficult to control. During the hydrothermal reactions, magnetic stirring was not applied since the container was sealed in a stainless steel autoclave and heated in a closed oven. Thus the reaction conditions in the Teflon container were not uniform, including the concentrations of precursor and ligands, reaction temperature, pressure, etc. The differences in reaction conditions might result the wide size distribution.

In addition, the presence of amorphous precursor in TEM images was probably because of the improper purification process. As mentioned in Section 2.2, in order to remove the unreacted precursors in products, the dispersant and precipitate should be chosen some solvent which could dissolve the precursors. However, toluene and ethanol are both poor solvent for bismuth nitrate. As a result, the mixture of toluene and ethanol is not capable for removing the unreacted bismuth nitrate.

Chapter 4. Bismuth Nanoparticles Synthesis by Liquid Phase Reaction

4.1. Mechanism of Polyacrylic Acid-Polystyrene (PAA-PS) Diblock Copolymer Templates

Hydrothermal reaction process is not an appropriate method to make bismuth nanoparticles. In order to improve the uniformity of the bismuth nanoparticles, I used a PAA-PS diblock copolymer template to control the morphology of bismuth nanoparticles. Fig. 4.1 is the schematic of the template, which is designed by X. Pang[64].

Generally, copolymer templates have fixed structures and sizes, which strongly control the sizes and shapes of nanoparticles. Differently from the ligands, the mechanism of the templates is that the core block of the template contains several functional groups which will absorb the precursor molecule during the synthesis process. When the precursor starts reacting, the crystal nucleus will form inside the core of the templates and finally nanocrystals will grow inside the template. On the other hand, the shell block is usually functional group free, which will not absorb any precursor molecule. Thus when the crystals grow up and fully occupy the core of the templates, the growth will be stopped by the shell of the templates.

In the PAA-PS diblock copolymer templates, the PAA core contains many hydroxyl functional groups, which can absorb precursor molecule. Fig. 4.2 is the molecular formula of PAA. Each repeat unit of PAA has one hydroxyl functional group, which can absorb one precursor molecule. The molecule weight of PAA is 72n, where n is the degree of polymerization. The diameter of the core of the template is 6 nm, which means

the nanoparticles inside the templates will have a diameter of 6 nm. The shell of the template is PS, which works as ligands and makes the particles dispersing in toluene well.

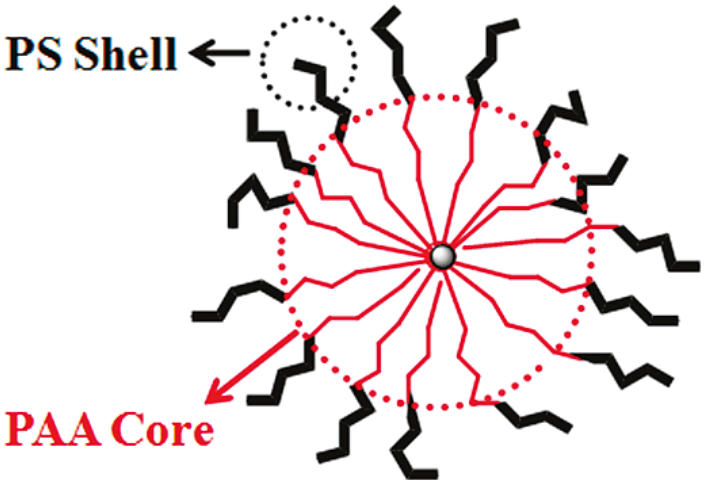

Fig. 4.1 A schematic of the PAA-PS diblock copolymer template.

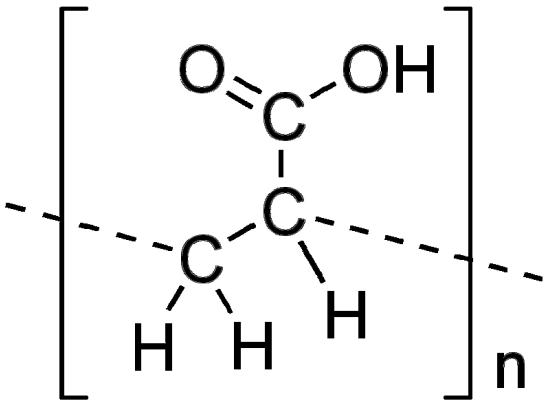

Fig. 4.2 the molecular formula of PAA.

4.2. Liquid Phase Reaction with PAA-PS Diblock Copolymer Templates

Liquid phase reaction process was chosen for synthesizing bismuth nanoparticles with PAA-PS diblock copolymer template, since the reaction conditions are more easily to

control than that of hydrothermal reactions. 10 mg PAA-PS diblock copolymer template was dissolved in 10 ml DMF. The molecular weight of the repeat unit of PAA is 72 and the weight ratio of PAA and PS in the template is 1:1. Thus there was 5mg PAA in the 10 mg template, which was 0.07 mmol. In order to make sure the bismuth nanoparticles could fully occupy the template, I added excessive precursors to the template/DMF solution. The mole ratio of precursor to template was 5:1. Thus 0.35 mmol (169.8 mg) bismuth nitrate pentahydrate was added to the template/DMF solution. The liquid phase reactions were performed in a three-mouth flask with reflux as Fig 2.3 shows. Magnetic stirring was applied during the reactions to ensure the uniformity of reaction conditions. Reflux was implemented by a condenser cooled by water and argon protection was applied to prevent the bismuth nanoparticles from oxidation. The reaction temperature was set at 153℃, which is the boiling point of DMF at atmosphere. Two reaction time was attempted, 3 and 7 hours. The purification process was the same as the hydrothermal process. Fig. 4.3 is the XRD result of the bismuth nanoparticles obtained by liquid phase reaction with templates. Similarly, the wide peaks indicate the nanoscale of the bismuth particles.

Fig. 4.4 is the TEM images of bismuth nanoparticles synthesized with templates for 3 and 7 hours. Heavily aggregations were existed in the 7-hour reaction. The possible reason is that DMF is not a good solvent for bismuth nitrate. Therefore there were still many precursors suspended in DMF during the reactions and the undissolved precursors could not be absorbed by the templates. Even they might not able to grow on the nucleus inside the templates, since they might be even larger than the templates. As results, they

grew outside the templates and formed particles larger than 6 nm. Since the particles outside the templates were surfactant free, they would be very easy to get aggregated.

Since the template would absorb the precursor molecule during the reactions, the templates would help the nanocrystals to nucleate. Thus the growth of bismuth nanoparticles inside the templates is faster than that outside the templates. The reason why heavily aggregation did not appear in the 3-hour reaction might because the precursor outside the template did not have enough time to react. Also the mixture of toluene and ethanol used for purification was not capable to remove the unreacted precursor, which explains why the TEM image of Fig 4.4 (a) is not clear. The amorphous precursors covered on the bismuth nanoparticles prevented the TEM from focusing.

In order to ensure that most nanoparticles growing inside the templates, we need dissolving the precursor thoroughly. I tried different precursors and solvents to find the best precursors and solvents for liquid phase reactions. Since the template works only when it dissolves in the solvent, it limits the choice of solvents and to enable the reaction of precursors, the boiling point of the solvent should be higher than 120℃. So far, I have tried DMF, 1-Octadecene (ODE), ethylene glycol, tri-n-octylphosphine oxide (TOPO) and oleylamine, which are some common organic solvents used for nanocrystals synthesis[62, 65-68]. The solubility of templates in were observed by laser scattering method qualitatively, whose mechanism is that the laser is invisible during its route in a uniform solution, while it will be scattered by small particles in a suspension and become visible. By observing the laser through the solution, I could determine whether the templates

were dissolved. The result was that only DMF can well dissolve the PAA-PS diblock copolymer templates. Thus DMF is an indispensible solvent for this synthesis process.

Since bismuth nitrate does not dissolve in DMF well, I tried some other precursors: bismuth chloride, bismuth acetate, bismuth carbonate and bismuth oxide with stearic acid. Bismuth chloride has similar chemical properties as bismuth nitrate. Thus it forms a cloudy suspension in DMF. When a laser beam illuminated through the solution, the beam was slightly scattered. Bismuth acetate and bismuth carbonate are two organic salts, and their structure are listed in Fig 4.3. These two chemicals are both insoluble in DMF, since they formed opaque suspensions in DMF. The last trial of precursor was the bismuth-stearic acid, which was prepared by mixing 100 mg bismuth oxide and 1 g stearic acid at 80℃. Stearic acid was melted and formed light yellow solution with bismuth oxide. Then 10 ml DMF was added to the solution, and another opaque suspension formed as well.

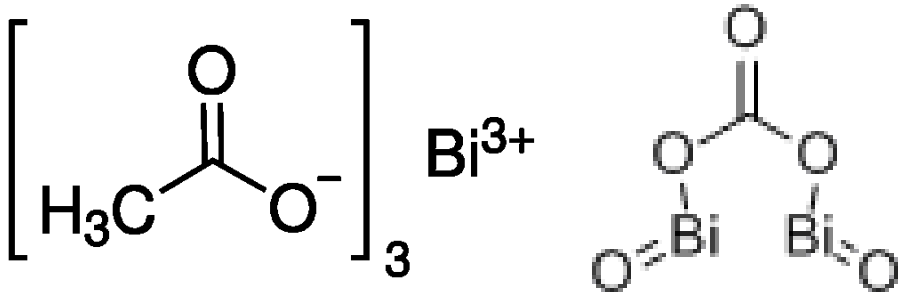

(a) (b)

As a result, none of the bismuth precursors are soluble in DMF. Thus I tried some mixture of DMF and other solvents. Ethylene glycol was reported as a good solvent for bismuth nitrate[69], so I dissolved 2.4 g (0.01 mol) bismuth nitrated pentahydrate in 20 ml ethylene glycol at 80℃ under magnetic stirring until all the precursors were dissolved and formed a transparent colorless solution with a concentration of 0.5mmol/ml. Then 0.7 ml bismuth nitrate/ethylene glycol solution was added in the 10 mg/10 ml template/DMF solution forming a transparent colorless solution as well. Since the precursors were excessive compared with the templates, the growth of bismuth crystals outside the templates should be lowered, so I lowered the reaction temperature to 140 ℃ and set the reaction time for 4 hours. To better remove the unreacted precursors, I used DMF as dispersant and ethylene glycol as precipitant for purification, because the bismuth particles with PS corona could disperse in DMF very well and bismuth nitrate could also partially dissolved in DMF, while ethylene glycol is a good solvent for bismuth nitrate while it could make the bismuth particles precipitate, since PS cannot dissolve in ethylene glycol.

Fig. 4.5 is the TEM images of bismuth nanoparticles with refined synthesis process. Compared with Fig. 4.4 the morphologies of bismuth nanoparticles were better controlled. Aggregations were almost eliminated and unreacted precursors were well removed. Nevertheless, the sizes and shapes of the bismuth nanoparticles were still not uniform. This might be because DMF is a good solvent for both PAA and PS. When the templates dissolve in DMF, the sizes and shapes will change and fail in controlling the

morphologies of nanoparticles strongly. To avoid this problem, some poor solvent for PAA is needed to confine the sizes and shapes of templates.

Here benzyl alcohol was chosen as the poor solvent for PAA. The ratio of DMF to benzyl alcohol was 9:1. The experimental procedure was that dissolving bismuth nitrate in ethylene glycol to form a 0.5 mmol/ml precursor solution and dissolving 10 mg PAA-PS diblock copolymer templates in a mixture of 9 ml DMF and 1 ml benzyl alcohol. 0.7 ml precursor solution was added to the template solution. The reaction was a liquid phase reaction at a temperature of 140℃ for 4 hours.

To obtain better morphologies of bismuth nanoparticles, the purification process was improved as well. First, the 10 ml product suspension was diluted in 50 ml DMF in a glass vial and placed in an ultrasonic bath for 15 minutes to make sure the bismuth particles covered with PS corona could well dispensed in DMF and avoid the possible tangles between PS chains. After ultrasonic, the product suspension was shaken for 1 minute and stood for 5 minutes. At that time, the large particles which grew outside the templates precipitated, while the small particles inside the templates and the unreacted precursors were still suspending in the DMF. Then 10 ml of the suspension was transferred to a 15 ml centrifuge tube and 1 ml ethylene glycol was added. The centrifuge tube was shaken for 1 minute and heated in an oven at a temperature of 80℃ for 5 minutes to ensure that the unreacted precursor was fully dissolved. The suspension was centrifuged at a speed of 3600 rpm for 5 minutes. After centrifuge, the precipitates were dispensed in 10 ml DMF again and 1 ml ethylene glycol was added. The centrifuge process was repeated for twice.

Fig 4.6 shows the morphologies of bismuth nanoparticles synthesized with the presence of benzyl alcohol. The morphologies of the bismuth nanoparticles were better controlled this time. The particles size was about 6 nm and the shapes of the particles were nearly uniform. Nevertheless, there were some overlaps of the particles in the TEM images, which was because the concentration of TEM solution was too high to make all the particles separate from each other. Also shapes of some particles were not sphere, which probably because the ethylene glycol had some negative impact on the structure of the templates. The important thing is that the Fig. 4.6 (c) shows that most of the particles obtained were almost uniform in morphologies and all of them were smaller than 10 nm. Therefore these bismuth nanoparticles were ready for further use.

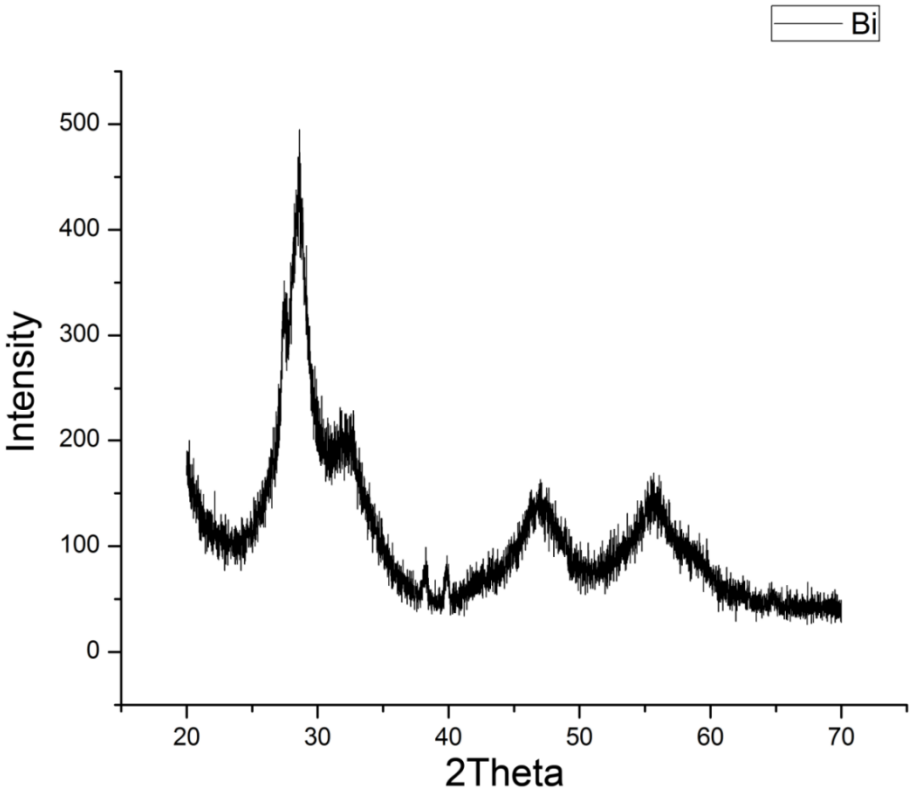

Fig. 4.3 XRD result of bismuth nanoparticles synthesized by liquid phase reaction with PAA-PS diblock copolymer templates.

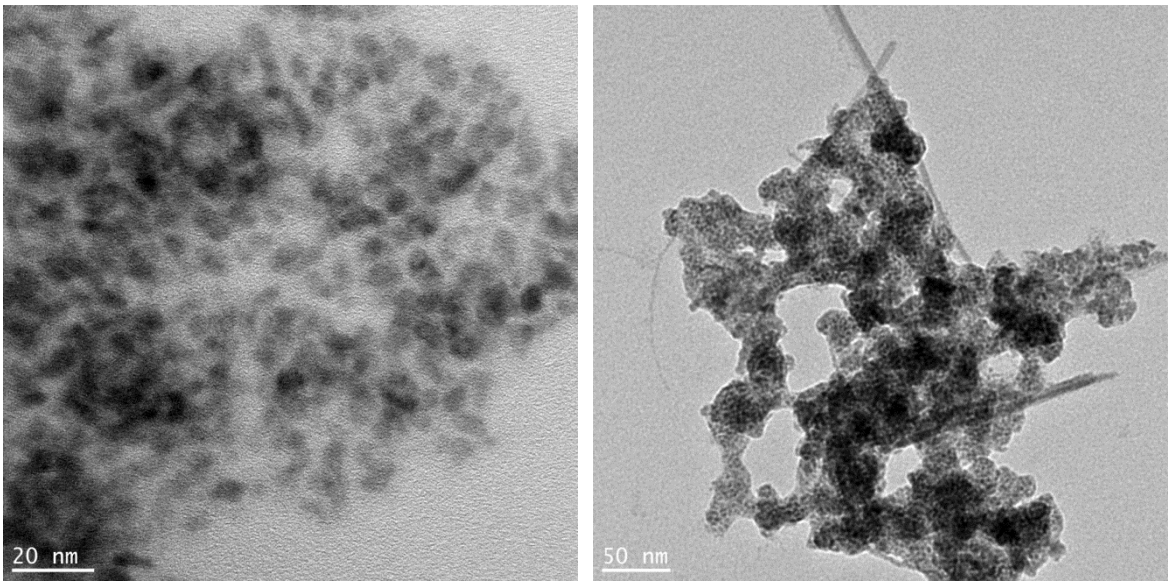

(a) (b)

Fig. 4.4 TEM images of Bi nanoparticles synthesized with PAA-PS diblock copolymer template with different reaction times (a) 3 hours (b) 7 hours

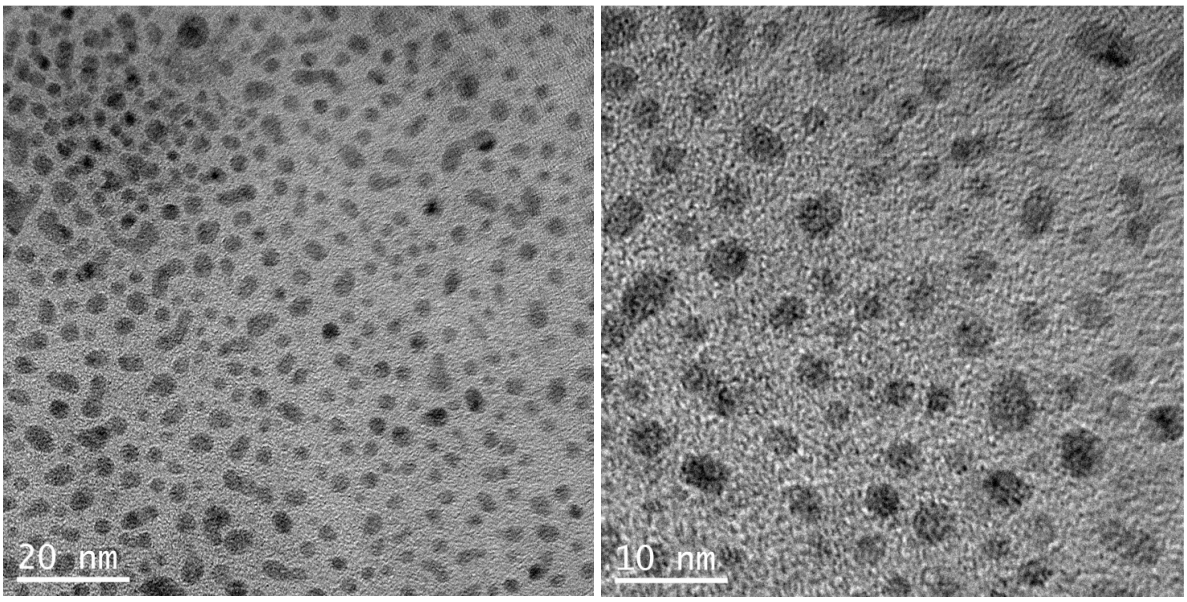

(a) (b)

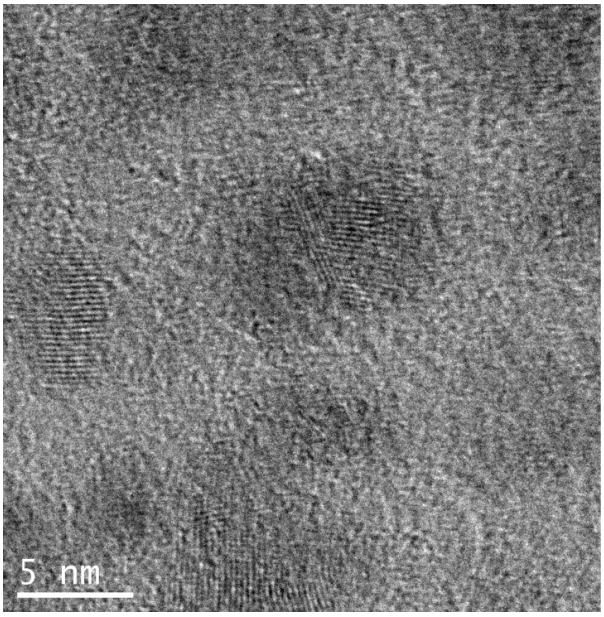

(c)

Fig. 4.5 TEM images of Bi nanoparticles synthesized with PAA-PS diblock copolymer templates in a mixture solvent of DMF and ethylene glycol and purified with DMF and ethylene glycol.

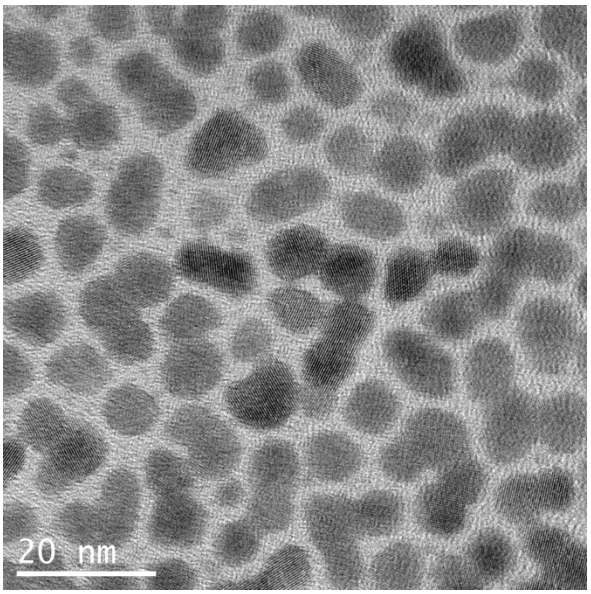

(a)

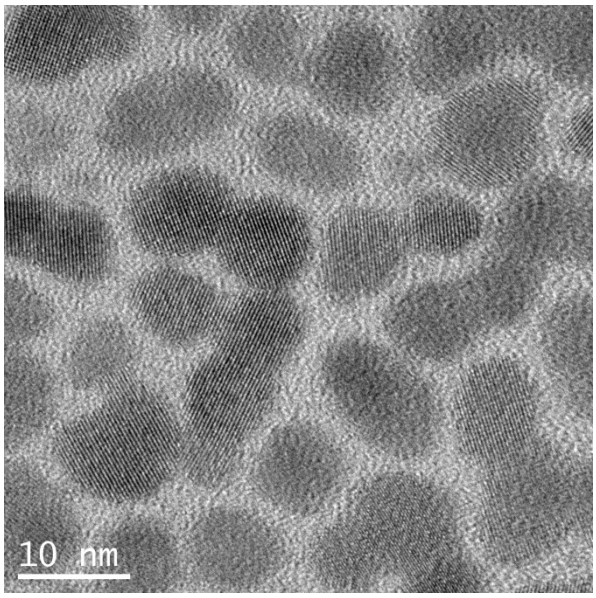

(b)

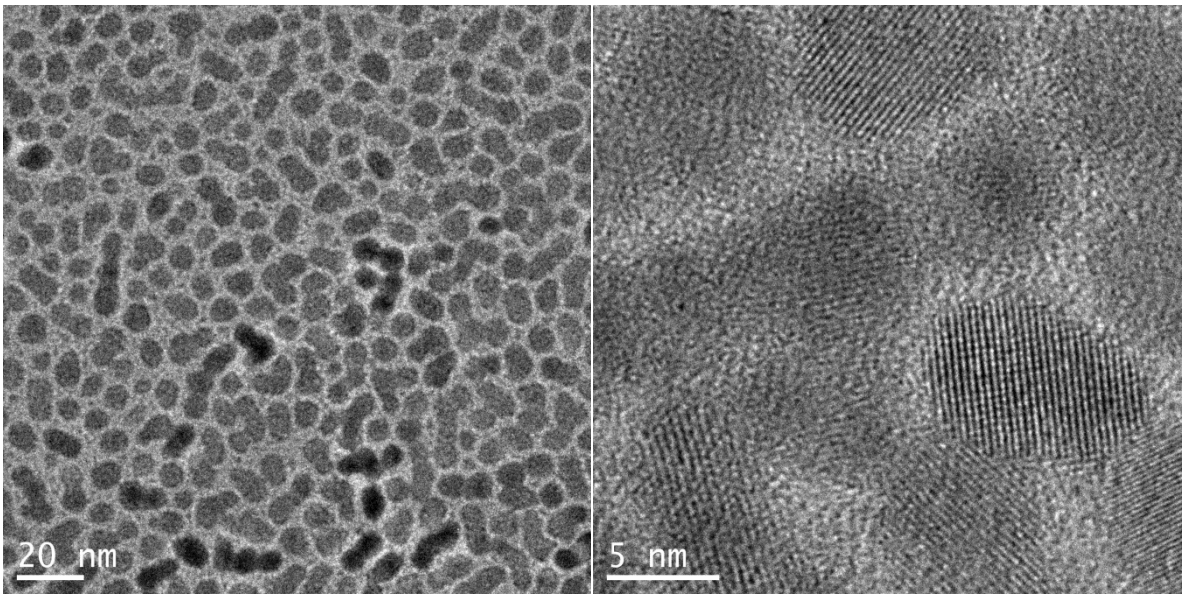

(c) (d)

Fig 4.6 TEM images of Bi nanoparticles synthesized with PAA-PS diblock copolymer templates in a mixture solvent of DMF, benzyl alcohol and ethylene glycol and purified with DMF and ethylene glycol.

4.3. Results and discussions

Liquid phase reaction with PAA-PS diblock copolymer templates is a promising method to synthesize uniform bismuth nanoparticles. The templates are able to absorb the precursor molecule, and could accelerate nucleation. To well control the morphologies of bismuth nanoparticles, the reaction conditions are critical, like solvent, reaction time and temperature, purification process.

Solvent: Pure DMF is not a good solvent for the precursor bismuth nitrate, but it still could be used in hydrothermal reactions since the high pressure and temperature increase the solubility of bismuth nitrate in DMF, while in liquid phase reactions the solubility would be a problem that the undissolved precursor would not enter the templates to form

nanocrystals. With 7% ethylene glycol in DMF, the precursor could be well dissolved. Reactions in the solvent of DMF and ethylene glycol, the precursor molecule could enter the template and grow inside. On the other hand, DMF is a good solvent for both of the two blocks of the templates, in which the template could not keep its size and shape and fail to make the particles uniform. Adding 10% benzyl alcohol which is a poor solvent for PAA, could make the PAA block of the template shrink and the size and shape of the template are fixed. Finally, the morphologies of nanoparticles will be better controlled.

Reaction time and temperature: According to thermodynamics, the precursors cannot be completely reacted, so in order to make the nanoparticles fully occupy the templates, excessive precursors were added, which brought a problem that the precursors outside the templates might nucleate and form crystals as well. Moreover, the crystals outside the templates are usually larger than the ones inside the template since they grow without any confinements. A low reaction temperature and a proper reaction time could eliminate the nanocrystals grow outside the templates. Here 140℃ and 4 hours are an appropriate reaction temperature and time for bismuth nanoparticles synthesis.

Purification process: Purification is a key to obtain uniform nanoparticles. Diluting the original product solution and applying ultrasonic on the diluted solution would make the nanoparticles well disperse. A proper combination of dispersant and precipitant would remove most unreacted precursors and particles with large differences in size to the target particles. Here DMF and ethylene glycol are the suitable dispersant and precipitant respectively. The ratio of them is 10:1.

Chapter 5. Tests of Thermoelectric Properties

5.1. Fabrication of bismuth films

To test the thermoelectric properties of the bismuth nanoparticles synthesized with PAA-PS diblock copolymer templates, they need to be made into films. I tried three methods to make bismuth films with its nanoparticles, spin-coating, drop cast and hot press.

5.1.1 Spin-coating

The spin-coating was performed on glass substrates with a spin-coating machine. The glass substrates (Fisher Scientific) were cut into 1''X1" squares and well cleaned. First rubbing the substrates with a lint free cloth and then washed in soap aqueous, di-water, isopropanol and acetone in an ultrasonic bath for 15 minutes respectively. The cleaned substrates were dried in an oven at a temperature of 80℃. The purified bismuth nanoparticles with PAA-PS diblock copolymer templates were dispersed in toluene at a concentration of 30 mg/ml. 40 µl bismuth suspensions was drawn up by a micropipette and dropped on the glass substrate. The substrates were slightly inclined with tweezers to make the drop cover all of the glass substrates. Then the substrates were spun at a speed of 1000 rpm for 30 seconds. The different films were fabricated by spinning for 1, 3, 5 and 10 layers. Due to the limitation of spin-coating, a large fraction of the suspensions were wasted, so the thickness of the films was thin and the films were not compact.

5.1.2 Drop Cast

Drop cast is a common method to make thick films. In my work, drop cast was performed on the same glass substrates as the spin-coating process. In order to make the

films more compact, I used a 60mg/ml suspension. 40 µl of the suspension was dropped on a substrate and dried at room temperature. Fig 5.1 is the images of films under optic microscope. The dark areas of the images are the bismuth nanoparticles. To make the film conductive, the particles should contact with each other and form a continuous film. Thus, the 2-layer film is still too thin.

Therefore bismuth films of more layers were fabricated, however the films cracked when the layers added up to 3, as Fig. 5.2 (a) shows. Another 150 mg/ml bismuth nanoparticle suspension was used to drop cast films. Nevertheless the cracks appeared even in single layer films, as Fig. 5.2. (b) shows.

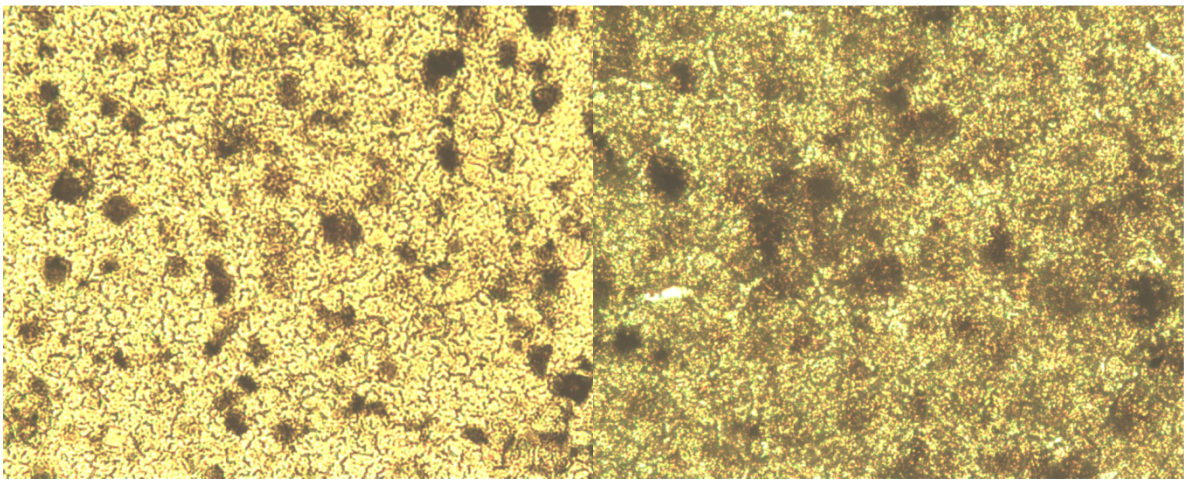

(a) (b)

Fig. 5.1 Optical microscopic images of bismuth films fabricated by drop cast, (a) 1-layer film, (b) 2-layer film.

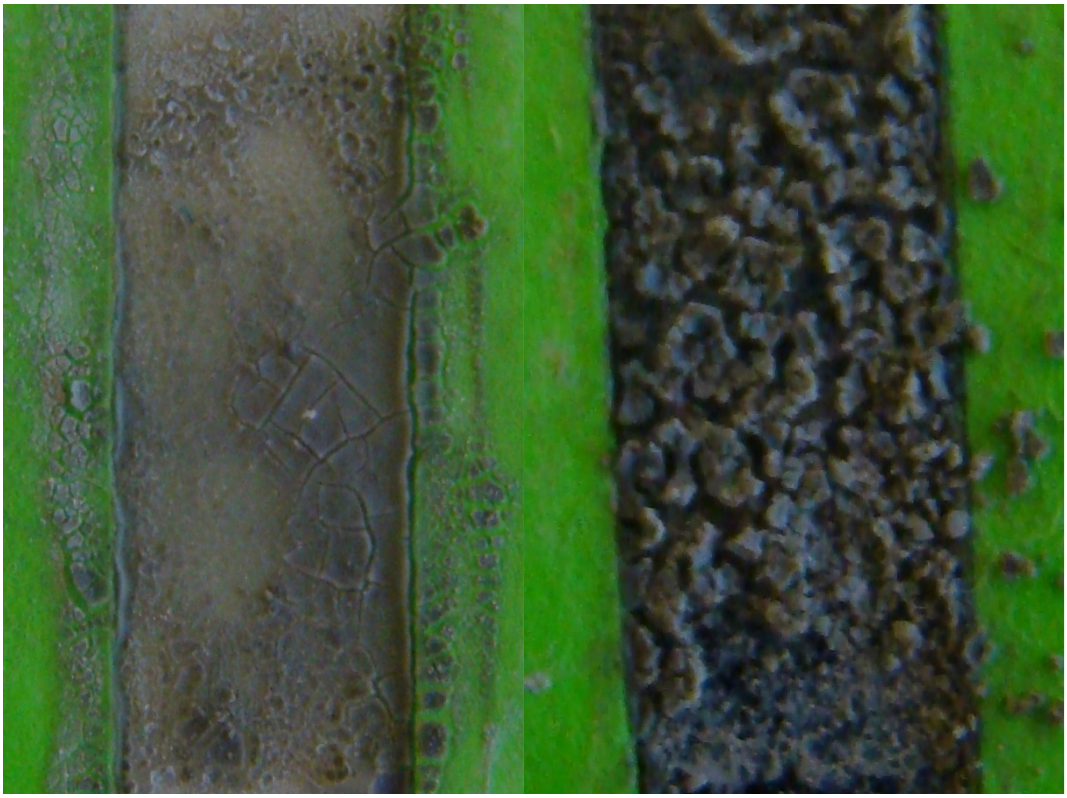

(a) (b)

Fig 5.2. The bismuth film fabricated by drop cast with bismuth-toluene suspensions of different concentration and layers. (a) 3-layer bismuth film fabricated with 60 mg/ml suspension, (b) single layer bismuth film fabricated with 150 mg/suspension.

5.1.3 Hot Press

Since neither spin-coating nor drop cast is a good method to make bismuth films, hot press was tried to make compact continuous films. The purified bismuth nanoparticles with PAA-PS diblock copolymer templates were dried in a vacuum oven at 80℃ and then well ground. 0.4 g ground bismuth powders were put into a half-inch (0.0127 m) die, which was sprayed some silicon nanoparticles beforehand in order to make the bismuth film easy to be taken out. The hot press temperature was set at 170℃, at which PS were melt. The press force was set at 600 lbf, which was 2669 N. Since the area of the film is

$1.27X10^{-4}$ m^2, the pressure applied on the film was $2.1X10^7$ Pa. The temperature and pressure were kept for 5 minutes to ensure the bismuth particles well connected to each other. The pressed film was polished with a sand paper and finally a 0.59 mm bismuth film with a diameter of 0.0127 m was obtained.

5.2. Thin film annealing

Since the bismuth nanoparticles were synthesized with PAA-PS diblock copolymer templates, the electrical conductivity of the bismuth films might lowered by the PS between particles. In order to improve the electrical properties, the PS should be burned before testing the electrical conductivity. Thermo gravimetric analysis (TGA) of the bismuth thin film was applied to determine the anneal temperature. Fig 5.4 is the TGA result of bismuth nanoparticles covered with PS. The green curve in the Fig 5.4 is the weight of bismuth nanoparticles vs temperature, and the blue curve is the derivative of the weight of bismuth nanoparticles vs the temperature. The weight of the bismuth nanoparticles decreases rapidly at 200℃, and in the blue curve, there is a sharp peak at 200℃ indicating the degradation temperature of PS. Fig. 5.5 is the TGA result of pure metallic bismuth. There is no peak in the curves while the weight of bismuth increases gradually after 300℃, which indicates the oxidation temperature of metallic bismuth. Based on these two TGA results, 250℃ is a proper temperature to anneal the bismuth thin films, at which the PS can be burned while the film will not get oxidized. The annealing was implemented in an oven at 250℃. In addition, since the annealing temperature was only 50℃ higher than the degradation temperature of PS, the samples were annealed for 4 hours to ensure the thoroughness of the removal of PS.

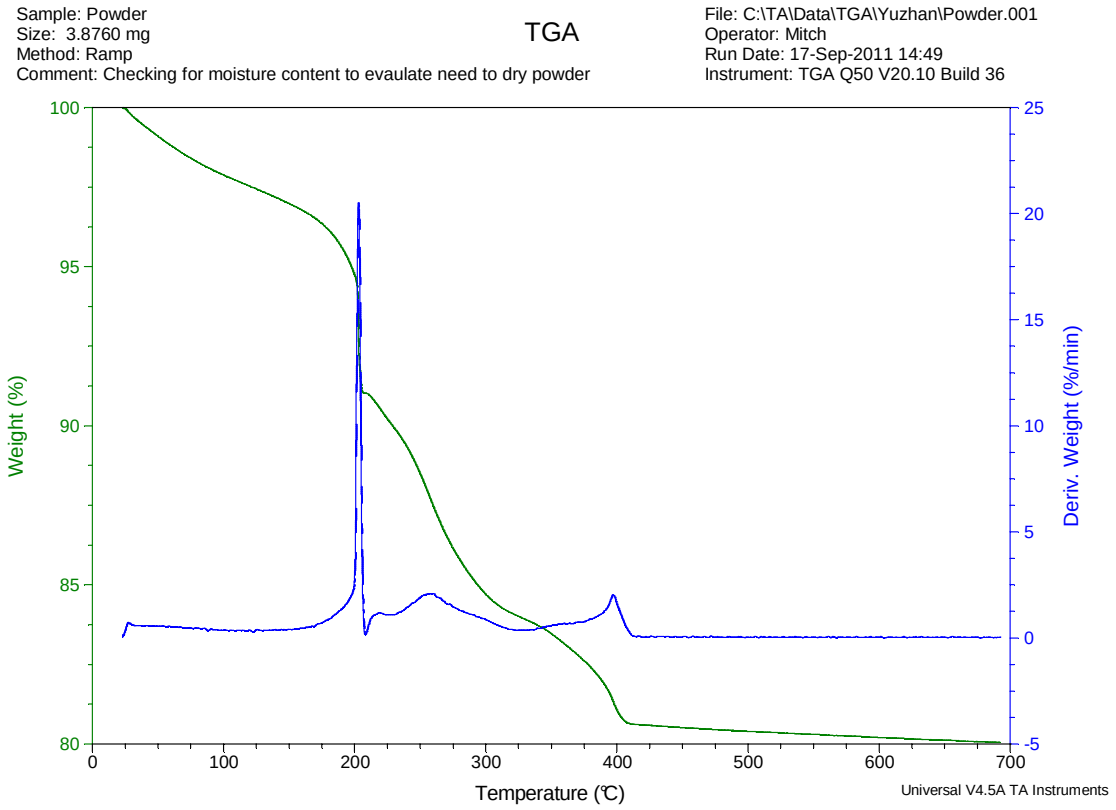

Fig 5.4. TGA result of bismuth nanoparticles with PAA-PS diblock copolymer templates, in which the peak at 200℃ indicates the degradation temperature of PS.

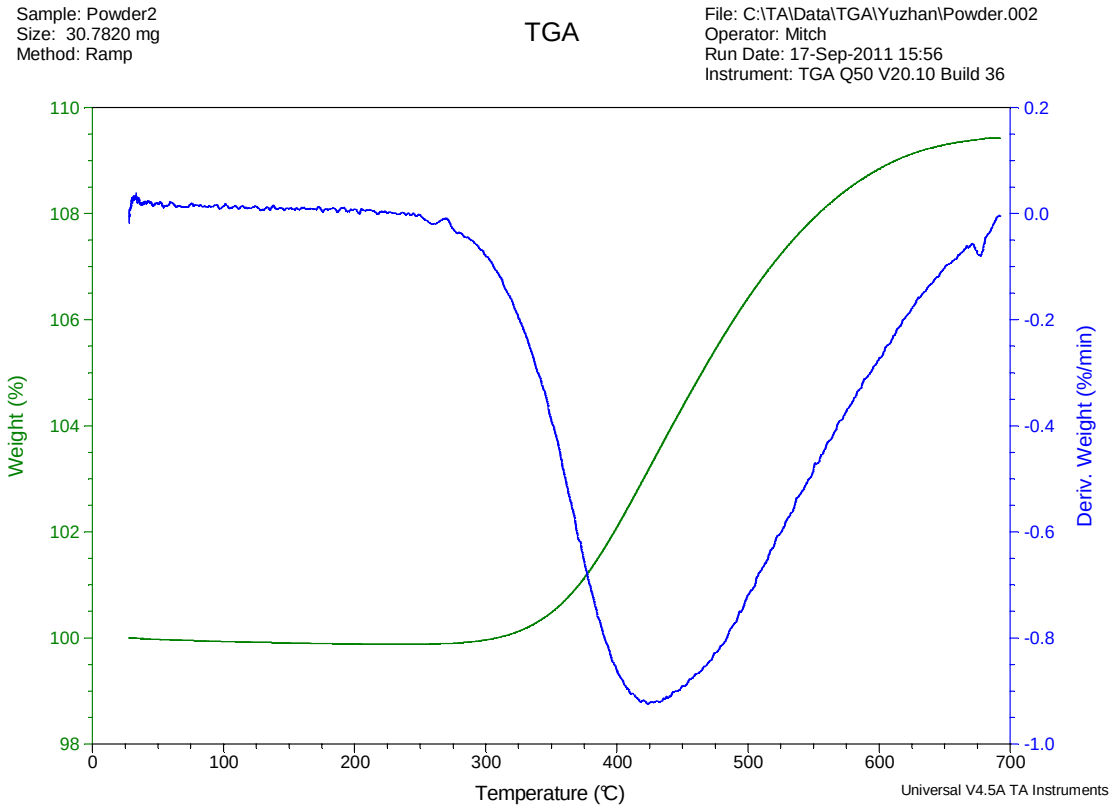

Fig. 5.5. TGA result of pure metallic bismuth, in which the weight of bismuth began to increase after 300℃, which is the oxidation temperature of bismuth.

5.3. Electrical conductivity testing

The electrical conductivity of the bismuth film was tested by a Jandel RM2 four-point probe measurement. The I-V curve of bismuth thin film I measured is as Fig 5.6 shows. The resistivity ρ can be obtained by:

$$\rho = 2\pi s R F, \qquad (5.1)$$

where s is the distance between the point two and point three as Fig 2.11 shows, R is the resistance obtained from measurement and F is a geometric correction factor, which can be expressed as:

$$F = \frac{t}{2s}\left(ln\frac{\sinh(t/s)}{\sinh(t/2s)}\right)^{-1}, \quad (5.2)$$

where t is the thickness of the sample. s is a parameter of the measurement which is 1.591 mm, the thickness of my sample is 0.59 mm. Substituting the values with the variables in equation 5.2, F is 0.261. R is measured by the four-point probe measurement, Fig. 5.3 is the I-V curve of my bismuth thin film fabricated by hot press. As the result shows, the I-V curve is linear, and the slope of the curve stands for the resistance of the sample, which is 2 KΩ. Substituting the value of F, R and s into equation 5.1, the resistivity of bismuth thin film fabricated with the bismuth nanoparticles is 5.2 Ωm. Compared with the electrical conductivity of bulk bismuth, which is 1.29μΩm[70], the electrical resistivity of the thin is 4000 times of that of the bulk one. The relationship of electrical conductivity and resistivity is

$$\sigma=1/\rho \quad (5.3)$$

Thus the electrical conductivity of the bismuth thin film is 0.19 S/m, which is 1/4000 of that of the bulk bismuth.

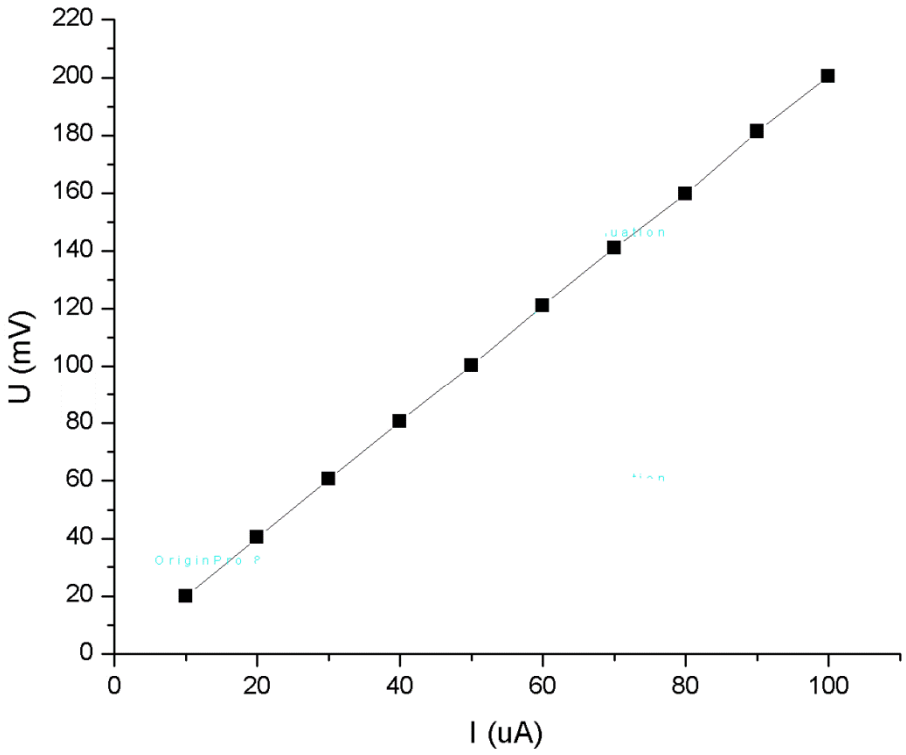

Fig. 5.6 The I-V curve of the bismuth film measured by a Jandel RM2 four-point probe measurement. The dots on the figure stand for the measured results and the solid curve is the fitting line.

Chapter 6. General Conclusions

The bismuth nanocrystals were studied in my research. Hydrothermal reaction and liquid phase reaction were two main method used for bismuth nanoparticle synthesis. For hydrothermal, the ligand and template free reaction produces large bismuth particles (the diameters were about several micrometers) with irregular shapes. The effect of ligand was notable, which can control the morphology of bismuth particles. With the presence of oleic acid during the hydrothermal reaction, the sizes of bismuth particles were all less than 50 nm and the shape of the particles was cubic.

Since the high temperature and pressure in the Teflon container during hydrothermal reactions would increase the solubility of bismuth, the solubility of precursors did not cause problems in controlling the morphology of bismuth particles. However in the liquid phase reaction, the pressure equaled atmospheric pressure and the precursor bismuth nitrate only partially dissolved in DMF, which resulted that the morphologies of bismuth particles were not uniform and heavily aggregated even with the presence of PAA-PS diblock copolymer templates. Since the templates only dissolve in DMF, DMF should be a majority of the solvent. Many other precursor were tried including bismuth nitrate, bismuth chloride, bismuth acetate and bismuth carbonate and so further, but none of them dissolve in DMF fully. Finally, the solubility problem was solved by dissolving precursors in the mixture of ethylene glycol and DMF. In addition, by adding 10% benzoyl alcohol as poor solvent for PAA, the structures of the templates could be more stable and better control the morphologies of bismuth particles. Finally, nearly uniform bismuth nanoparticles covered PS coronas with a diameter of 6 nm were synthesized.

The bismuth nanoparticles with synthesized with templates were further fabricated into thin films. Since the films were used for measure the thermoelectric properties of bismuth nanoparticles, they should be compact to ensure the electrical conductivity. Due to the nanoscale size of the particles, the thickness of the films should be large enough to make the particles contact with each other. The films fabricated by spin coating were too thin to be conductive. Drop cast could fabricate thicker films. However, the films cracked when the thickness of the films increased. Hot press was a suitable method for making uniform compact bismuth nanoparticle thin film, which could be used for further measurement.

The bismuth films fabricated by hot press were annealed before measurement in order to remove the PS coronas among bismuth nanoparticles, which would reduce the electrical conductivity of the films. The electrical conductivity of bismuth nanoparticles was decreased to 0.19 S/m. The thermal conductivity of the bismuth film was not tested due to the limitation of equipment. I used transient electrothermal technique[71] to test the thermal conductivity of the bismuth thin film, which requires the rod-like shape of the sample, while the bismuth film is disk-like. Nevertheless, the total thermal conductivity is expected to decrease greatly as well, since the electron thermal conductivity decreases with electrical conductivity and lattice thermal conductivity decrease significantly in nanocrystals. To measure the total thermal conductivity and Seebeck coefficient, further investigation is required.

References

1. D. M. Rowe, *CRC handbook of thermoelectrics*, CRC Press **(1995)**

2. T. C. Harman, P. J. Taylor, M. P. Walsh and B. E. LaForge, Science. 297, 2229 **(2002)**

3. T. J. Seebeck, Abhandlungen der Deutschen Akademie der Wissenschafren zu Berlin. 265 **(1822)**

4. F. J. DiSalvo, Science. 285, 703 **(1999)**

5. J. C. A. Peltier, electrique, Ann. Chim. 1, 371 **(1834)**

6. D. M. Rowe, *Thermoelectrics handbook: macro to nano*, CRC/Taylor & Francis **(2006)**

7. W. Thomson, Proceeding of the Royal Society of Edinburgh. 3, 91 **(1851)**

8. L. D. Hicks and M. S. Dresselhaus, Physical Review B. 47, 12727 **(1993)**

9. L. D. Hicks and M. S. Dresselhaus, Physical Review B. 47, 16631 **(1993)**

10. L. D. Hicks, T. C. Harman and M. S. Dresselhaus, Appl. Phys. Lett. 63, 3230 **(1993)**

11. L. D. Hicks, T. C. Harman, X. Sun and M. S. Dresselhaus, Physical Review B. 53, R10493 **(1996)**

12. N. S. Popovich, Czechoslovak Journal of Physics. 55, 739 **(2005)**

13. L. Zhang and D. J. Singh, Physical Review B. 80, 075117 **(2009)**

14. L. Nordström and D. J. Singh, Physical Review B. 53, 1103 **(1996)**

15. C. Kittel, *Introduction to solid state physics*, Wiley **(2005)**

16. A. F. Ioffe, *Semiconductor thermoelements, and Thermoelectric cooling*, Infosearch, ltd. **(1957)**

17. T. C. Harman, M. J. Logan, B. Paris and E. H. Lougher, J. Electrochem. Soc. 105, C161 **(1958)**

18. Champnes.Ch, P. T. Chiang and P. Parekh, Can. J. Phys. 43, 653 **(1965)**

19. Mountval.Aj and G. Abowitz, J. Am. Ceram. Soc. 48, 651 **(1965)**

20. Stavitsk.Ts, V. A. Long and B. A. Efimova, Soviet Physics Solid State,Ussr. 7, 2062 **(1966)**

21. I. Kudman, Journal of Materials Science. 7, 1027 **(1972)**

22. M. Kobayashi, K. Ikoma, K. Furuya, K. Shinohara, H. Takao, M. Miyoshi, Y. Imanishi, T. Watanabe and Ieee, *Thermoelectric generation and related properties of conventional type module based on Si-Ge alloy*, I E E E **(1996)**

23. N. Savvides and D. M. Rowe, J. Phys. D-Appl. Phys. 14, 723 **(1981)**

24. J. P. Heremans, V. Jovovic, E. S. Toberer, A. Saramat, K. Kurosaki, A. Charoenphakdee, S. Yamanaka and G. J. Snyder, Science. 321, 554 **(2008)**

25. G. A. Slack, in CRC handbook of thermoelectrics, Edited D. M. Rowe, CRC Press, **(1995)**, pp.

26. J. L. Feldman and D. J. Singh, Physical Review B. 53, 6273 **(1996)**

27. M. Fornari and D. J. Singh, Physical Review B. 59, 9722 **(1999)**

28. D. Mandrus, B. C. Sales and V. Keppens, *Filled skutterudite antimonides: Validation of the electron-crystal phonon-glass approach to new thermoelectric materials*, **(1997)**

29. G. S. Nolas, D. T. Morelli and T. M. Tritt, Annual Review of Materials Science. 29, 89 **(1999)**

30. B. C. Sales, D. Mandrus and R. K. Williams, Science. 272, 1325 **(1996)**

31. D. J. Singh and I. I. Mazin, Physical Review B. 56, R1650 **(1997)**

32. A. M. Guloy, R. Ramlau, Z. J. Tang, W. Schnelle, M. Baitinger and Y. Grin, Nature. 443, 320 **(2006)**

33. V. L. Kuznetsov, L. A. Kuznetsova, A. E. Kaliazin and D. M. Rowe, Journal of Applied Physics. 87, 7871 **(2000)**

34. A. Saramat, G. Svensson, A. E. C. Palmqvist, C. Stiewe, E. Mueller, D. Platzek, S. G. K. Williams, D. M. Rowe, J. D. Bryan and G. D. Stucky, Journal of Applied Physics. 99, **(2006)**

35. T. Ikeda, V. A. Ravi, L. A. Collins, S. M. Haile and G. J. Snyder, J. Electron. Mater. 36, 716 **(2007)**

36. M. Salavati-Niasari, M. Bazarganipour and F. Davar, J. Alloy. Compd. 489, 530 **(2010)**

37. D. Dragoman and M. Dragoman, Appl. Phys. Lett. 91, **(2007)**

38. H. Li, X. F. Tang, X. L. Su and Q. J. Zhang, Appl. Phys. Lett. 92, **(2008)**

39. G. Zhang, X. Lu, W. Wang and X. Li, Chem. Mat. 19, 5207 **(2007)**

40. W. J. Xie, X. F. Tang, Y. G. Yan, Q. J. Zhang and T. M. Tritt, Journal of Applied Physics. 105, **(2009)**

41. A. M. Rao, X. H. Ji and T. M. Tritt, MRS Bull. 31, 218 **(2006)**

42. X. W. Wang, H. Lee, Y. C. Lan, G. H. Zhu, G. Joshi, D. Z. Wang, J. Yang, A. J. Muto, M. Y. Tang, J. Klatsky, S. Song, M. S. Dresselhaus, G. Chen and Z. F. Ren, Appl. Phys. Lett. 93, **(2008)**

43. Y. Q. Cao, X. B. Zhao, T. J. Zhu, X. B. Zhang and J. P. Tu, Appl. Phys. Lett. 92, **(2008)**

44. X. F. Tang, W. J. Xie, H. Li, W. Y. Zhao, Q. J. Zhang and M. Niino, Appl. Phys. Lett. 90, **(2007)**

45. Z. W. Zhang, Y. Wang, Y. Deng and Y. B. Xu, Solid State Commun. 151, 1520 **(2011)**

46. K. C. See, J. P. Feser, C. E. Chen, A. Majumdar, J. J. Urban and R. A. Segalman, Nano Lett. 10, 4664 **(2010)**

47. B. Zhang, J. Sun, H. E. Katz, F. Fang and R. L. Opila, ACS Appl. Mater. Interfaces. 2, 3170 **(2010)**

48. B. Poudel, Q. Hao, Y. Ma, Y. Lan, A. Minnich, B. Yu, X. Yan, D. Wang, A. Muto, D. Vashaee, X. Chen, J. Liu, M. S. Dresselhaus, G. Chen and Z. Ren, Science. 320, 634 **(2008)**

49. X. B. Zhao, X. H. Ji, Y. H. Zhang, T. J. Zhu, J. P. Tu and X. B. Zhang, Appl. Phys. Lett. 86, 3 **(2005)**

50. A. I. Hochbaum, R. Chen, R. D. Delgado, W. Liang, E. C. Garnett, M. Najarian, A. Majumdar and P. Yang, Nature. 451, 163 **(2008)**

51. B. Poudel, Q. Hao, Y. Ma, Y. C. Lan, A. Minnich, B. Yu, X. A. Yan, D. Z. Wang, A. Muto, D. Vashaee, X. Y. Chen, J. M. Liu, M. S. Dresselhaus, G. Chen and Z. F. Ren, Science. 320, 634 **(2008)**

52. M. G. Kanatzidis, Chem. Mat. 22, 648 **(2009)**

53. N. Peranio, O. Eibl and J. Nurnus, Journal of Applied Physics. 100, **(2006)**

54. D. R. Lide, in CRC handbook of chemistry and physics: a ready-reference book of chemical and physical data Edited CRC Press, **(2004)**, pp. 4

55. R. A. Laudise, in 50 years progress in crystal growth: a reprint collection, Edited R. Feigelson, Elsevier, **(2004)**, pp. 185

56. C. Chen, J. Cheng, S. Yu, L. Che and Z. Meng, Journal of Crystal Growth. 291, 135 **(2006)**

57. J. A. Gonzalo and C. A. López, *Great solid state physicists of the 20th century*, World Scientific **(2003)**

58. M. Scheele, N. Oeschler, K. Meier, A. Kornowski, C. Klinke and H. Weller, Advanced Functional Materials. 19, 3476 **(2009)**

59. F. Gao, Q. Lu, S. Xie and D. Zhao, Advanced Materials. 14, 1537 **(2002)**

60. H. Yu, P. C. Gibbons and W. E. Buhro, Journal of Materials Chemistry. 14, 595 **(2004)**

61. W. G. Lu, Y. Ding, Y. X. Chen, Z. L. Wang and J. Y. Fang, J. Am. Chem. Soc. 127, 10112 **(2005)**

62. L. Zhao, X. Pang, R. Adhikary, J. W. Petrich, M. Jeffries-El and Z. Lin, Advanced Materials. 23, 2844 **(2011)**

63. A. L. Patterson, Physical Review. 56, 978 **(1939)**

64. X. C. Pang, L. Zhao, M. Akinc, J. K. Kim and Z. Q. Lin, Macromolecules. 44, 3746 **(2011)**

65. Q. J. Guo, H. W. Hillhouse and R. Agrawal, J. Am. Chem. Soc. 131, 11672 **(2009)**

66. L. Zhao, X. Pang, R. Adhikary, J. W. Petrich and Z. Lin, Angewandte Chemie International Edition. 50, 3958 **(2011)**

67. S. Li, M. S. Toprak, H. M. A. Soliman, J. Zhou, M. Muhammed, D. Platzek and E. Müller, Chem. Mat. 18, 3627 **(2006)**

68. W. P. Hong and K. J. Lee, Synthesis. 33 **(2005)**

69. W. Wang, J. Goebl, L. He, S. Aloni, Y. Hu, L. Zhen and Y. Yin, J. Am. Chem. Soc. 132, 17316 **(2010)**

70. O. N. E. A. N. S. Committee, in Handbook on lead-bismuth eutectic alloy and lead properties, materials compatibility, thermal-hydraulics and technologies Edited OECD Nuclear Energy Agency, **(2007)**, pp. 80

71. J. Guo, X. Wang and T. Wang, Journal of Applied Physics. 101, 063537 **(2007)**